

Viking era water ice clouds

Leslie K. Tamppari
Jet Propulsion Laboratory
M/S 264-538
4800 Oak Grove Dr.
Pasadena, CA 91109
phone: (818) 393-1226
fax: (818) 393-4530
email: leslie.tamppari@jpl.nasa.gov

Richard W. Zurek
Jet Propulsion Laboratory
M/S 183-335
4800 Oak Grove Dr.
Pasadena, CA 91109
phone: (818) 354-3725
email: rwz@rich.jpl.nasa.gov

David A. Paige
University of California, Los Angeles
Dept. of Earth and Space Science
595 Charles E. Young Dr. East
3806 Geology Bldg.
P.O. Box 951567
Los Angeles, CA
90095-1567
phone: (310) 825-4268
email: dap@thesun.ess.ucla.edu

Number of manuscript pages: 27
Number of figures: 7 (12 pages)
Number of tables: 1
Key words: Mars; Mars, atmosphere

Abstract

We have spatially and temporally determined and mapped the water ice clouds for 1.25 Martian years using the Viking Infrared Thermal Mapper (IRTM) data. Our technique compares brightness temperatures in the 11 and 20 μm IRTM channels, utilizing the 11 μm water ice absorption feature. A complication arises due to the surface non-unit, wavelength-dependent emissivities. We developed a technique for removal of this effect. Using a surface thermal model, we calculate brightness temperatures and their differences in the IRTM channels resulting from the surface emissivity effect alone. These are then subtracted from the measured brightness temperatures, yielding brightness temperatures with solely atmospheric contribution. Our ability to identify water ice clouds in the infrared provides potential new information about particle size and physical processes by comparing these clouds to those seen in visible wavelengths. We found that water ice clouds are more widespread and frequent than had been previously recognized, with the northern spring and summer times being the cloudiest on Mars. We identified the southern and northern solstice season upwelling branches of the Hadley cell which have been shifted 15-20° southward from model predictions. Additionally, the transition between the two branches occurred later in time than model predictions. We observed the onset of the north polar hood which is confined to longitude 120-200. We did not find evidence for a south polar hood, nor any evidence for interannual variability within our data set. We observed storm zone generated clouds over Acidalia Planitia.

Keywords: Mars; Mars, atmosphere

Viking era water ice clouds

1. Introduction

Telescopic observations from as early as 1796 have shown the presence of “white” or “bluish” features in the atmosphere which have been interpreted as water ice clouds [H. Flaugergues, cited in *Capen and Martin*, 1971]. Since then, suspected water-ice clouds have been observed by spacecraft at Mars and telescopes on Earth or in orbit around it (i.e., the Hubble Space Telescope). Most recently, the Mars Pathfinder camera (IMP) observed predawn bluish clouds [*Smith et al.*, 1997], while the Mars Global Surveyor (MGS) camera [MOC; *Malin et al.*, 1992] and the Thermal Emission Spectrometer [TES; *Christensen et al.*, 1992] even now are observing water ice clouds in the Martian atmosphere.

Despite the early observations that water ice clouds existed and were on occasion widespread, these clouds were not thought to play a key role in the atmospheric circulation, and their role in the Martian water cycle was uncertain. The amounts of water involved in the formation of the observed ice clouds was small and so the latent heating associated with them was regarded as negligible, especially when compared to the direct atmospheric heating that could be achieved when even minor amounts of dust were suspended in the atmosphere [*Zurek et al.*, 1992]. Because the most widespread hazes appeared to be relatively thin, radiative effects also tended to be neglected, away from the polar regions and other than for surface fogs.

With regard to the water cycle, it was unclear to what extent the seasonal transport of water ice contributed to the overall annual redistribution of water on Mars [*Jakosky and Haberle*, 1992]. Certainly, condensation appeared to limit the vertical extent of most of the water vapor in an atmospheric column [*Davies*, 1979, *Jakosky*, 1985], and there

appeared to be a lowering of the water ice cloud base in northern spring and summer [Jaquin *et al.*, 1986] which could affect the Mars water cycle by amplifying seasonal exchange between the atmosphere and surface [Kahn, 1990]. It was also suggested that water condensation on dust grains could remove dust from the atmosphere immediately below detached hazes seen above the planet's limb [Kahn, 1990]. However, complete scavenging of the atmospheric dust in a vertical column by ice cloud formation was regarded to be principally a polar process dominated by formation of carbon dioxide clouds.

This conventional view of water ice clouds as relatively less important in the role of climate was challenged by Clancy *et al.* [1996 and in several meeting papers thereafter]. They proposed that water ice cloud formation provided in some seasons a global control of the vertical distribution of atmospheric dust. By removing dust and its associated solar heating, ice condensation could play a major role in the global circulation and in the transport of dust, as well as water.

In this hypothesis, the present eccentricity of the orbit of Mars and the occurrence of aphelion during late northern spring radiatively leads to colder temperatures during northern spring and summer, resulting in more frequent and widespread water ice clouds. The formation of these clouds causes gravitational settling of ice particles in the rising branch of a cross-equatorial Hadley circulation, which then limits water to the northern hemisphere. The effectiveness of this trapping of water is amplified by the simultaneous scavenging of atmospheric dust, which keeps atmospheric temperatures low by removal of the radiatively active dust. While aspects of this hypothesis are still being debated and investigated, orbital eccentricity is clearly a potent mechanism for possible climate change, past and present, since it suggests that the "wet" hemisphere will be the one with aphelic summer whenever the orbit is significantly elliptical.

Clancy *et al.* [1996] also argued for significant interannual variability during the past decade, contrasting more recent cold (and presumably dust free) northern spring and

summers observed using ground-based microwave spectrometers with the Viking period. While this temperature difference with the Viking period may be an artifact of the atmospheric temperatures derived from the Viking IRTM [*Richardson, 1998; Wilson and Richardson, in press*], the question remains as to whether there were fewer water-ice clouds during the Viking period, when the atmosphere was observed to have a significant background dust loading. Note, however, that even if the atmosphere becomes warmer, it is not immediately obvious that the clouds may become spatially less extensive; they may for instance simply occur at a higher altitude.

Furthermore, large-scale atmospheric dynamics may dictate some aspects of the global distribution of clouds: rising air will cool adiabatically and form preferred regions for clouds, whereas sinking air will warm, tending to produce cloud-free zones. Since the cross-equatorial (Hadley) circulations on Mars are expected to vary strongly in latitude with season, so too should the cloudy and cloud-free zones.

In this paper we re-examine the distribution and seasonal variation of clouds during the Viking period. Visual images of clouds have previously been characterized by French *et al.* [1981], Kahn [1984], and Jaquin *et al.* [1986]. We use the Viking IRTM data set which is also a global data set, but which is sensitive to different cloud properties. When viewing near-nadir, clouds may be more evident at IR wavelengths during the middle of the day, when the temperature contrast between the cloud and surface is typically large. In principle the IR measurements also have the potential to estimate cloud height and total cloud opacity, even for near-nadir viewing geometry. However, the spectral contrasts used to detect clouds in the thermal IR are also affected by atmospheric dust and by variable surface emissivities at these wavelengths. These surface emissivity effects became obvious when Christensen and Zurek [1984] tried to extend their cloud detection method to the global IRTM data set and found that many of the “cloud” maps had a high correlation with surface albedo (e.g., a perpetually cloud-free Syrtis Major). With the derivation of a surface emissivity map from the IRTM data [*Christensen, 1998*] it is now

possible to assess the importance of this artifact. Thus, our focus here is to remove these factors and to estimate cloud extent conservatively. The resulting data base will be useful to those modelling the Mars water cycle, including the role of water ice clouds. Furthermore, it can be used to study interannual variability through comparisons with results from the MGS TES, currently acquiring data at Mars, and from the Pressure Modulator IR Radiometer (PMIRR), now in flight to Mars aboard the Mars Climate Orbiter.

In section 2, we discuss our method of determining the presence of water ice clouds in the Martian atmosphere using the IRTM data set. This section includes a discussion of the impact of the surface spectral emissivities and the surface model used to estimate their effect. In Section 2 a cloud detection scheme is devised that takes advantage of the usual IR spectral contrast of a water-ice cloud and compares it to the spectral signature that would result if the cloud were not there. Section 3 discusses potential complications arising from dust in the atmosphere and other limitations of the cloud detection scheme proposed here. Section 4 is a presentation of our water ice cloud maps with a description of the spatial and temporal variation of these clouds. Finally, section 5 contains our conclusions.

2. Approach

2.1. Viking Infrared Thermal Mapper (IRTM) data

We used the Viking IRTM data set to search for water ice clouds. The IRTM instrument observed thermal emission from Mars in five wavelength (λ) bands [*Chase et al.*, 1978]. The spectral responses for the five thermal channels are shown in Fig. 1e. While all channels, except the 15 μm carbon dioxide (CO_2) channel, were designed to measure the Martian surface temperature, only the 7 μm channel (T_7) was fairly insensitive

to atmospheric aerosols (dust and water ice particles). Consequently, atmospheric water ice clouds and dust can be identified by comparing the signal in the different IRTM spectral bands.

Between Viking Orbiter 1 (VO1) and Viking Orbiter 2 (VO2), a little over two Mars years-worth of data were obtained, from June 1976 to July 1980. The L_s range (areocentric longitude of the sun, a seasonal parameter for which $L_s=0$ is the start of northern spring) extended from 84° in the first Mars year to 142° in the third [Snyder, 1977; Snyder and Moroz, 1992]. We will concentrate on the period from $L_s=84^\circ$ in the first Mars year to $L_s=170^\circ$ in the second Mars year, due to the more extensive coverage during this period. As of this writing, the Viking data set is the only continuous data set available that covers a substantial period of time (> 1 Mars year) from which a climate study can be performed.

We note a few other aspects of the Viking IRTM data set. First, the Viking orbiters took data in a manner such that 360° of longitude were covered by the spacecraft “walking” around the planet. As a result, it took $\sim 15^\circ$ of L_s to cover a full 360° degrees of longitude. Second, the southern summer, referred to as the dusty season, exhibited widespread dust clouds during the Viking mission with two planet encircling dust storms having $\tau_{9\mu\text{m}} \geq 0.6$ (estimated $\tau_{\text{vis}} \geq 1.5$), starting at $L_s=206.4$ and $L_s=274.2$ [Briggs *et al.*, 1979, Martin and Zurek, 1993, Zurek and Martin, 1993, Martin and Richardson, 1993]. For comparison and reference, the Mariner 9 observations covered primarily the winter season ($L_s= 290^\circ - 0^\circ$), and a planet encircling dust storm ($\tau_{\text{vis}} \geq 2$) was in process during a substantial part of that time [Leovy *et al.*, 1972]. Consequently, the first water ice cloud identification was very late in the Mariner 9 mission.

2.2. Detection of water ice clouds

Water ice clouds can be detected in the Viking IRTM data set by differencing the 11 and 20 μm channels [Hunt, 1979, Christensen and Zurek, 1984]. This technique makes use of a broad water absorption feature which spans roughly 10-30 microns (Fig. 1d); this spectral feature was first exploited by analysis of Mariner 9 IR Interferometer Spectrometer [IRIS; Curran *et al.*, 1973]. The 11 μm channel is more strongly affected by the water ice absorption than the 7, 9, and 20 μm channels. Fig. 1c shows a water ice cloud over the Tharsis ridge seen in a Mariner 9 IRIS spectrum. This identification of a water ice cloud was consistent with clouds shown in the concurrent Mariner 9 television photograph of the same region [Curran *et al.*, 1973]. This spectrum differs from the one taken in the lower Arcadia region, for which concurrent television photograph data showed no clouds (Fig. 1a). Fig. 1b shows a spectrum with a dust cloud absorption. Note that the 11 μm and 20 μm channels are both affected by the dust cloud, the 7 μm channel is not affected at all, and the 9 μm channel is most strongly affected, due to the strong dust absorption at that wavelength. The shape and location of the water ice and dust absorption features make it possible to distinguish between these two atmospheric aerosols, under most circumstances, but spectral contrast does depend upon particle size and for dust upon composition.

Christensen and Zurek [1984] studied twelve equator-to-north pole scans that were taken late in the Viking mission. They interpreted negative $T_{11}-T_{20}$ differences as evidence for polar haze clouds and an Olympus Mons cloud. When they applied this technique to the full IRTM data set, they found many clouds, particularly over the low-thermal inertia regions at lower altitudes, suggesting the influence of cross-equatorial Hadley circulation and perhaps Walker circulation. However, there were also striking correlations with surface albedo features, which were suspected to be due to surface emissivity effects (see below), particularly over dark regions like Syrtis Major. This was not unexpected since Christensen [1982] had previously found that surface emissivity is closely related to surface albedo.

2.2.1. Surface spectral emissivities (ϵ_λ)

The radiances observed by the Viking IRTM are the sum of surface emission, of atmospheric emission from various levels in the atmosphere and of surface and atmospheric emission scattered into the line of sight, all attenuated over their respective paths by atmospheric absorption and scattering out of the line of sight. For wavelengths outside the main carbon dioxide gas vibrational bands, the top-of-atmosphere radiances overwhelmingly consist of surface emission, unless there are water ice or dust clouds and hazes in the atmospheric path. The surface emission itself is the product of temperature-dependent emission and an emissivity which reflects surface composition and particle size. In principle, one hopes for enough information to determine the spectral emissivity of the surface and the spatial distributions and optical properties of the aerosols. That is not possible from the Viking IRTM data, with its on-planet viewing geometry and low spectral information content, especially since the single IRTM atmospheric carbon dioxide band (near 15 μm) provides only modest constraints on atmospheric temperatures and thus on aerosol irradiance.

Given this situation, Christensen [1998] carefully determined surface emissivities (as convolved with the IRTM bandpasses--see Fig. 1) by examining data during periods when atmospheric dust loading was low. The data were also screened qualitatively by examining the T_{11} - T_{20} spectral contrasts to remove cases that were likely to have significant water ice cloud contributions. He used only daytime data, which reduced the effect of subpixel anisothermality and consequently surface emissivity uncertainties. The period he examined was $L_s=0$ -180.

Christensen [1998] observed the T_7 , T_9 , T_{11} , and T_{20} brightness temperatures for a given lat/lon bin. He then assumed the highest brightness temperature value was equal to the kinetic temperature of the surface, implicitly assigning an emissivity of unity to that channel, usually T_7 . Assuming this kinetic temperature, he calculated the appropriate

radiance and convolved that with the IRTM band shapes to produce synthetic radiances. By ratioing these synthetic radiances to the measured radiances, the different spectral emissivities were derived (Fig. 2).

2.2.2 IRTM Brightness Temperatures for a Clear Atmosphere

Given Christensen's [1998] surface emissivity map and given surface kinetic temperature, a scheme can be devised (Fig. 2) whereby atmospheric hazes can be detected even when there are non-unit surface emissivities contributing to the radiances observed by IRTM. Such kinetic temperatures cannot be determined accurately from the IRTM data themselves when aerosols are present, even given the surface emissivities, mainly because the (vertical) variation of temperature with aerosol opacity is not known.

Paige *et al.* [1994] devised a surface thermal model which reproduces the IRTM 20- μm brightness temperatures (T_{20}) using surface albedo A_s [Pleskot and Miner, 1981] and thermal inertia I_s [Palluconi and Kieffer, 1981], consistently assuming no significant atmospheric aerosol contribution to the surface energy balance. The model's synthetic 20- μm IRTM radiance is divided by Christensen's [1998] ϵ_{20} to yield an estimate of the kinetic surface temperature T_k in the absence of aerosols (T_k^{NC}). With this cloud-free surface temperature, other IRTM brightness temperatures can be estimated and differenced to provide the spectral contrasts for those wavelength pairs commonly used to detect dust and water ice clouds; these will be nonzero even when clouds are absent due to non-unit and variable surface emissivities. Thus, instead of comparing the observed T_7 - T_9 and T_{11} - T_{20} spectral contrasts to zero [for dust: Martin, 1986; Martin and Richardson, 1993] or to an arbitrary threshold [for water-ice: Christensen and Zurek, 1984] independent of surface location, cloud detections can be improved by comparing observed differences to those which would result only from variable surface emissivities.

The surface thermal model of Paige *et al.* [1994] was run to generate synthetic 20- μm IRTM radiances as a function of season, latitude, and longitude (in $2^\circ \times 2^\circ$ bins). These 20 μm radiances were then divided by the 20 μm emissivities [Christensen, 1998] on a lat/lon, bin by bin basis and convolved with the 20 μm band pass to produce a kinetic surface temperature (T_k) for the same seasonal and spatial bins. T_k was then convolved with the other band passes and multiplied by the appropriate emissivities on a lat/lon, bin by bin basis and converted back to brightness temperatures. This process is diagrammed in Fig. 2. The modelled surface kinetic and IRTM brightness temperatures were restricted to ± 60 latitude, consistent with the original derivation of surface albedo and thermal inertia used in the Paige *et al.* thermal model .

2.2.3. IRTM data preparation

Observed brightness temperatures were also mapped onto $2^\circ \times 2^\circ$ lat/lon bins from 60S to 60N and averaged over 15° of L_s , roughly the amount of time required for a Viking Orbiter to walk around the planet, covering all longitudes. The $2^\circ \times 2^\circ$ binning provides the best combination of spatial coverage and resolution and is consistent with past determinations of surface thermal inertia and albedo. To achieve this mapping, the IRTM data examined here were constrained to have emission angles $< 60^\circ$ and spacecraft ranges between 3000 and 64000 km (in fact most data were taken at a range $< 37,000$ km for a field-of-view size < 3 degrees along a great circle). The data were also screened for out-of-bound points (i.e., values < 100 K or > 350 K or with formal errors > 2 K as reported in the IRTM data product). For observations meeting these criteria, brightness temperatures were assigned to the bin into which the field-of-view center fell; multiple values for a given wavelength in a bin were averaged together.

2.2.4 Cloud Signatures

The spectral differences from IRTM data, $T_{11}-T_{20}$ and T_7-T_9 , corresponding to the potential signatures of water ice and dust hazes, were computed for each lat/lon, L_s , and local-time bin and contrasted with the differences that would be produced by surface emissivity effects alone; e.g., $T_{11}^{NC}-T_{20}^{NC}$. An example map of this surface emissivity difference is shown in Fig. 3b where differences range from -5 K to some positive values. (Note that 11 and 20- μm emissivities were not determined for a few bins.) As expected [Christensen, 1982], these spectral difference variations are highly correlated with surface albedo, as in Acidalia Planitia (45N, 30W) and Syrtis Major (0N, 300W).

As indicated in Fig. 2, the signature of a water ice cloud is then identified by comparing the observed spectral difference, in T_{11} and T_{20} , with the spectral difference that would occur if there were no clouds:

$$\Delta T_{(C+S)} - \Delta T_S^{NC} = \Delta_w \leq \beta \quad (1)$$

The sign of Δ_w is determined largely by the sign of the difference between the effective ice cloud temperature and the surface temperature. During the day, $\Delta_w < \beta = 0$ indicates a water-ice cloud, since the surface is relatively hot. The nighttime situation is less straightforward, since the ground temperatures can be nearly the same or lower than the cloud temperatures for clouds that are relatively low in the atmosphere. To sidestep this nighttime ambiguity, only mid-day (10-14H; Martian day contains 24H) data are examined here, when the surface is expected to be significantly warmer than likely water-ice clouds. Furthermore, within the ± 60 latitude domain, comparisons are not made with those few bins for which the surface thermal model indicates significant CO_2 frost accumulation ($> 0.1 \text{ gm}^{-2}$).

A sample map of Δ_w is shown in Fig. 3c, with the modelled ground spectral signature (Fig. 3b) subtracted from the observed (Fig. 3a). Note that, unlike Fig. 3a, Δ_w

in Fig. 3c does not show a strong correlation with albedo features such as Acidalia and Syrtis planae.

2.2.5 Uncertainties in Δ_w

There are several sources of uncertainty in using $\Delta_w < 0$ as the signature of a daytime water ice cloud. There are observational uncertainties in the IRTM data themselves and artifacts produced by nonlinearities due to temperature variations in the IRTM field of view [Christensen, 1982]. There are uncertainties in the averaging of brightness temperatures in the binning procedure and the differencing of the brightness temperatures (rather than radiances), as in (1). These are all relatively small compared to the effect of, and therefore the uncertainty in, constructing the ΔT_s^{NC} difference in (1) and the possible effects of the water-ice (or dust) clouds on the real surface temperatures at the time of the IRTM observation. Eq. (1) implicitly assumes that the IRTM temperatures from which the surface emissivities were estimated and thus the modelled ground (kinetic) temperatures and derived surface albedo and thermal inertia are not affected by water-ice atmospheric clouds or by residual dust hazes present during the period when the surface properties were estimated. This assumption is not strictly true, and the resulting uncertainties must be taken into account.

It is important to remember that Eq. (1) does not formally remove the effect of non-unit surface spectral emissivity from the brightness temperature (spectral) differences. Instead, it provides a more realistic, spatially variable threshold against which to compare spectral signatures of potential clouds. Simultaneous retrieval of the surface and atmospheric properties is not possible from the IRTM data alone.

3. Detection difficulties

3.1. Dust in the atmosphere

We found that under certain conditions, dust in the atmosphere could be mistaken for water ice clouds by examining Δ_w . In order to understand these conditions more fully, we modelled both dust and ice clouds in the atmosphere, over varying surfaces. The model and cases studies are discussed below, followed by the results and implications.

A 1-D radiative transfer model [Paige *et al.*, 1994] was used to create $\Delta_w=(T_{11}-T_{20})_{(C+S)} - (T_{11}-T_{20})_S^{NC}$, for both water ice and dust clouds. This model was also used to create $\Delta_D=(T_7-T_9)_{(C+S)} - (T_7-T_9)_S^{NC}$, for both water ice and dust clouds. In this way, we could compare the effect of both cloud types in the (T_{11}, T_{20}) channel pair and the (T_7, T_9) channel pair (Fig. 4).

In our dust modelling we used a modified gamma (mod- Γ) distribution with two different dust compositions (Fig. 4), both of which were found to reproduce martian dust fairly well [Toon *et al.*, 1977, Clancy *et al.*, 1995]. Specifically, we used refractive indices for (1) 75% montmorillonite 219b and 25% basalt with mod- Γ parameters $\alpha=2$, $\gamma=0.5$ and a mode radius value of $r_m=0.4 \mu\text{m}$ [effective radius= $2.75 \mu\text{m}$; Toon *et al.*, 1977] and (2) palagonite [Roush *et al.*, 1994] extended to 25-30 μm using values from Snook [1999] with mod- Γ parameters $\alpha=1$, $\gamma=0.3$ and a mode radius value of $r_m=0.014 \mu\text{m}$ [effective radius= $1.8 \mu\text{m}$; Clancy *et al.*, 1995]. The Snook [1999] refractive indices were derived from the Mariner 9 IRIS data through an iterative process.

For the water ice cloud comparison modelling, we used the mod- Γ distribution with $\alpha=8$, $\gamma=3$, which corresponds to Deirmendjian's [1969] C.3 clouds [high altitude, polar, mother-of-pearl clouds; used in Curran *et al.*, 1973]. We generated three mode radius cases: 1, 2, and 4 μm .

For each set of dust and water ice characteristics, Δ_w and Δ_D temperature differences were computed for a variety of opacities and cloud temperatures. For the

initial modelling runs, the dust cloud visible opacity was varied from $\tau_{\text{vis}}=0.0-1.5$ and the dust cloud temperature from 210-255 K in 5 K increments. We also varied the water ice cloud opacity from $\tau_{\text{vis}}=0.0-1.5$ and the temperature from 160-250 K in 10 K increments. The surface temperature was held constant at 260 K and the emission angle (EMA) at 30° (emission angles for the IRTM data used vary between 0°-60°).

As shown above, non-unit surface emissivities contribute to the resulting signal and must be modelled as well. We studied representative surface emissivity cases. We separated the data into cases satisfying $\epsilon_{11} > \epsilon_{20}$, $\epsilon_{20} > \epsilon_{11}$, $\epsilon_7 > \epsilon_9$, and $\epsilon_9 > \epsilon_7$. For all four cases, we found the average (μ) and standard deviation (σ) of the ϵ_λ s in the pair. In case 1 (Fig. 4a,b), we used representative ϵ_λ values separated by not only the difference in their means, but separated further by 1- σ on each value. For example, the separation between ϵ_{11} and ϵ_{20} when $\epsilon_{11} > \epsilon_{20}$ was chosen to be:

$$(\mu\epsilon_{11} + \sigma_{11}) - (\mu\epsilon_{20} - \sigma_{20}) \quad (2)$$

In case 2 (Fig. 4c,d), we simply used representative ϵ_λ values separated by the difference in their means.

Fig. 4 shows the modelling results and Table 1 describes the symbol usage. Since we are interested in what dust conditions produce $\Delta_w < 0$, we have used different symbols for dust modelled with different surface emissivity characteristics, but have only used one symbol (+) for all water ice cloud results.

Fig. 4 shows that for water ice, in most cases, both Δ_w and Δ_D are negative. Only in cases with cloud temperature very close to the surface temperature was this not true. Increasing the cloud thickness tended to decrease the Δ_D signature faster than the Δ_w signature. Reducing the cloud temperature decreased the Δ_w signature faster than the Δ_D signature.

Fig. 4 shows that the Δ_w values generated using palagonite can reach nearly -3 K and those generated using Montmorillonite+basalt can reach nearly -5 K. Increasing the dust cloud thickness tended to change the Δ_w signature, which became increasingly

negative for $\epsilon_{11} > \epsilon_{20}$ (\diamond and Δ) and increasingly positive for $\epsilon_{20} > \epsilon_{11}$ (\square and \times). Reducing the dust cloud temperature tended to increase the Δ_D signature. Therefore, dust cases with $\epsilon_{11} > \epsilon_{20}$ (\diamond and Δ) could be confused with water ice clouds, using a negative Δ_W criterion.

The spectral contrast dependence on cloud opacity and temperature results from the different surface emissivities and the non-linearity of the Planck function. If the surface emissivities were uniformly unity, then Δ_W would always be positive for palagonite hazes and always > -1 K for Montmorillonite+basalt.

We examined where $\epsilon_{11} > \epsilon_{20}$ occurs on the surface of Mars. Fig. 5a shows the magnitude of each bin in which $\epsilon_{11} > \epsilon_{20}$, as a function of west longitude and latitude (60S-60N). Figs. 5b and 5c show those locations where the $\epsilon_{11} - \epsilon_{20}$ emissivity differences are larger than 0.0113 (case 2; 60S-60N) and 0.0367 (case 1), respectively. As shown, these maps have little correlation with the cloud maps. Additionally, the dust points that caused a signature of $\Delta_W < -1$ K were those with a dust opacity $\tau_{vis} > 0.3$. Finally, not shown in Fig. 5, we modelled a case with $\epsilon_{11} = \epsilon_{20}$. Again, when the dust opacity was $\tau_{vis} \leq 0.3$, the signature was $\Delta_W < -1$ K. Since the dust opacity in the Martian atmosphere during the Viking era, outside of dust storm times, is typically $\tau_{vis} < 0.4$ with a majority of these points having $\tau_{vis} < 0.2$ [Martin and Richardson, 1993], we conclude that dust will not be misidentified as water ice clouds in our process.

3.2. Selection of a water ice threshold value

The dominant sources of error are the uncertainty in the emissivity determination and the uncertain effects of the presence of airborne dust, both upon the surface emissivity derivation itself and upon the detection scheme for clouds. Uncertainties in the emissivity determination alone could introduce errors of nearly 3K [Christensen, 1998], but these errors are not random, they are fixed spatially. Even so, the modelling discussed in section 3.1. indicates that some threshold other than $\Delta_W < 0$ K is required even when

surface emissivity effects are taken into account. That modelling (e.g., Fig. 4) suggests a more modest threshold of $\Delta < -1\text{K}$.

To test the sensitivity to the chosen threshold, we examined a period in early northern summer, $L_s=95\text{-}110$ in year 2 of the Viking Orbiter observations (Fig. 6). The extent of the "water-ice clouds" was greater when the threshold was raised (less negative), but it was consistent with reasonable variations in the spatial extent of cloud opacity, rather than errors in the surface emissivity or the presence of dust hazes. In the maps to be shown below, water-ice clouds are defined by

$$\Delta_w < -1 \text{ K} \quad (3)$$

In Fig. 6, the top panel (a) shows Δ_w for all data in this seasonal bin. The middle panel (b) shows only the clouds with a temperature signature more negative than -2.9 K . The lower panel (c) shows the clouds with a temperature signature more negative than -1.0 K .

3.3. Other effects

We determined that CO_2 ice clouds in the Martian atmosphere will not be confused with water ice clouds, since CO_2 ice cloud particles are not expected to grow above $0.5 \mu\text{m}$ [Wood *et al.*, 1997]. In general, the atmosphere is warmer than the surface in the polar regions which will change the Δ_w signature of the water ice clouds to a positive value [e.g., Christensen and Zurek, 1994]. The study in this paper concentrates on latitudes between $\pm 60^\circ$, so this will not be a concern.

4. Map comparison and discussion

4.1. Presentation of all residual cloud maps

Below we present a description of the residual water ice cloud maps (Fig. 7) determined using the scheme described in Fig. 2 with a threshold value of $\Delta_w < -1\text{K}$. The Viking IRTM areal coverage is not global for all times of day in all seasons. However, as will be shown, clouds are seen to change within a latitude band as a function of season as well as changing in latitudinal placement and extent with season. Topographically forced clouds can often be seen, especially over Olympus Mons and the other Tharsis volcanoes, as well as Elysium Mons. In Fig. 7, black areas indicate a lack of data coverage for that season and white areas indicate data that were above the threshold value. The color scale extends from light blue ($\Delta_w < -1\text{K}$) to dark purple ($\Delta_w \leq -10\text{K}$).

There are some regions where a very cold temperature signature always appeared. For example, (45S, 125W), (45S, 45W), and (55S, 350W) among others, were such cases. These bins do not correspond to topographic highs, so it is not likely that they are orographically forced clouds. More likely, they are places where the surface emissivity has been imperfectly determined, resulting in an erroneous cloud signature. They were deleted from the data set, without affecting the general picture of the cloudiness, since there were only a handful of these bins.

A summary of the number of longitude bins containing clouds as a function of season and latitude is shown in Fig. 8, along with the coverage pattern.

A qualitative discussion of the cloudiness as a function of season is presented below.

4.2. Description of cloudiness

Aspects of the water-ice cloud distribution and its change with season are highlighted below.

4.2.1 $L_s = 80-185$ Year 1: Northern Summer

Longitudinal coverage was relatively sparse during this early part of the Viking mission when the orbiters were supporting the Viking landers operating on the surface of Mars. Water-ice clouds tended to occur at low latitudes especially in the vicinity of the Tharsis and Elysium highlands. Elsewhere, clouds were indicated on the northern rim of Hellas. A band of clouds appeared in northern mid-latitudes by late summer.

4.2.2 $L_s = 185-275$ Year 1: Northern Fall

This period showed high-latitude bands of water-ice clouds, more extensive perhaps in the north, but also present in the south. Some water-ice clouds in lower latitudes may have been missed due to the presence of dust hazes associated with the first of the major Viking period duststorms (1977a). Coverage of the southern hemisphere was much more complete starting at $L_s=245$ and continuing into northern winter and spring.

4.2.3 $L_s = 275 - 335$ Year 1: 1977b Dust Storm (Northern Winter)

The water-ice cloud detection scheme yielded widespread clouds in southern mid-latitudes after the start of the second, larger, and more opaque major duststorm observed by Viking (1977b). We believe this to be an artifact of the detection algorithm caused by an indirect effect of a very opaque dust haze ($\tau_{vis} \geq 3.75$), namely the tendency of such a haze to cool the surface during the day, so that the Martian surface was then decidedly cooler than predicted by the surface thermal model used to remove the surface emissivity effect. Thus, the cloud detection scheme (Fig. 2) is “over-correcting” which results in a

negative Δ_w signature even though water-ice clouds may not be present. Some of the indicated water-ice clouds may be just that, but it is difficult to tell without an ability to retrieve simultaneously for dust hazes and water ice clouds.

4.2.4 $L_s = 335 - 80$ Year 1: Late Northern Winter and Northern Spring

As the Viking orbiter coverage shifted northward and the 1977b duststorm abated, two cloud bands appeared and persisted through the vernal equinox, one perhaps associated with the northern storm tracks and the polar hood, particularly in the western hemisphere, and the other in southern mid-latitudes. In early spring water-ice clouds appeared to occur frequently and extensively north in a region (30S, 45W) north of Argyre Planitia. In mid-spring the clouds were associated with Tharsis, with the southern cloud belt almost absent. In later spring the water-clouds appeared at nearly all longitudes, with a well-established band in the northern tropics. The clouds were relatively more extensive near the major upland regions, including Arabia and Elysium. These regions were noted as cloudy for this season in later Mars years by James *et al.* [1994] using HST images.

4.2.5 $L_s = 80 - 185$ Year 2: Northern Summer

The cloudy zone in late spring and early summer was much less patchy than earlier and there was some suggestion of more opaque clouds (e.g., Elysium, $L_s=110$). While the large-scale pattern was similar to what was seen one Mars year earlier, there were differences, so that there are temporal variations in the water-ice cloud distribution. Later in northern summer, the cloudy zone seemed to move (i.e., be more restricted) to the near-equatorial latitudes, though locally concentrated near the high volcanoes (Olympus Mons, Tharsis, Elysium), again as in the previous Mars year. One prominent cloud feature, over

Arcadia Planitia (45N, 180-210W), persisted through the latter half of northern summer (140-180), and perhaps even extended to the east as summer ended.

4.3. Implications for Dynamics

By analogy with Earth, planetary-scale cloud patterns on Mars are expected to reflect at least three types of dynamical phenomena: First is the global overturning of air known on Earth as the Hadley circulation, which should give cloudy (clear) zones in regions where solar heating of the surface and atmosphere produce rising (sinking) motion and its attendant adiabatic cooling (warming). Second, orographic features can generate clouds as elevated terrain preferentially heats the atmosphere and draws air upslope, again producing adiabatic cooling. Third, cold air masses that form in the wintertime middle and high latitudes are often marked by extensive cloudiness. Models of these phenomena [Zurek *et al.*, 1992] indicate that they are of sufficient extent that they may be captured in the Viking IRTM data set analyzed here. Mesoscale phenomena (e.g., due to gravity waves or lee clouds downwind of sharp relief, like crater rims) are too small to be resolved. Fogs (i.e., very low-lying clouds) may not have sufficient thermal contrast to be detected, and may be outside the daytime window examined here.

4.3.1. Hadley Circulations

Models indicate the rising branch should be in the spring/summer hemisphere and the descending branch in the fall/winter hemisphere. Near equinox there may be two overturning cells, with rising air near the equator and sinking air a few 10's of degrees poleward in both hemispheres; this transition, however, may be brief or simply be a transition from one summer pattern to the opposite hemisphere's spring pattern. The most prominent development of a cloud zone in the IRTM cloud signatures derived here is the

transition between a late northern winter (after $L_s=335$) zone in southern mid-latitudes (centered near 45S) through a period with less frequent clouds occurring near the equator in early northern spring ($L_s=20-50$) to a cloudy zone in the northern tropics (see Fig. 7). This northern zone is quite prominent after mid-spring and persists through solstice until mid-summer. This suggests the annual reversal of the Hadley circulation occurred in early northern spring. This persistence into spring was also suggested by Mariner 9 data [e.g., Zurek *et al.*, 1992], but is later than most models would predict [Haberle and Jakosky, 1990]. The latitudes of the rising branch are qualitatively consistent with modeling [e.g., Houben *et al.*, 1997], though the extent and location of the rising branch depends on the distribution of dust suspended in the atmosphere as well.

The transition at the northern fall equinox is not seen in these cloud maps, possibly because of the two major dust storms that occurred, the first in early northern fall (southern spring, $L_s=206.4$) and the second at the start of northern winter (southern summer, $L_s=274.2$) (Martin and Richardson 1993).

4.3.2. Polar Hood Clouds; Storm Zones

Polar hoods are cloud zones which develop over the polar cap during late summer and which persist through winter, sometimes into early spring [Leovy *et al.*, 1972, Briggs and Leovy, 1974, James *et al.*, 1994]. Models [Hollingsworth *et al.*, 1996, Hollingsworth *et al.*, 1997] also suggest that there are preferred zones for winter storms to follow in mid-to-high latitudes, often combining the effects of strong latitudinal temperature gradients and large-scale topography at high latitudes. Incomplete observational coverage limits the ability to follow individual storm systems, and it is sometimes difficult to differentiate between the polar hoods and storm-cloud zones, since the low-pressure storm systems can pull polar air into lower latitudes [e.g., Briggs and Leovy, 1974].

While our technique of detecting clouds was not extended poleward of 60N and 60S, there are periods when the polar hoods extended south of 60N, perhaps associated with storm systems. The most convincing storm zone clouds were those over Acidalia Planitia during the $L_s=245-275$ period (the $L_s=275$ bin includes the start of the 1977b planet-encircling dust storm), as they appear detached from the polar hood clouds. Following a gap in coverage, clouds are also seen in these regions in the $L_s=335-20$ period, when storms are still active [Barnes, 1980]. After this period, the few clouds that occurred in northern mid-latitudes appeared to be linked to topography (e.g., northeastern Tharsis).

Clancy *et al.* [1996] observed clouds between 30-60S during northern spring ($L_s=68$), which they interpreted as the southern polar hood. James *et al.* [1994] also saw evidence for a south polar hood at this season, in this case extending equatorward to 40S. The cloudy zone in the maps derived here suggests a mid-latitude belt prior to $L_s=30$, distinct from a possible polar hood. While we suggested that this could be the rising branch of the Hadley circulation, it could also be a southern storm track given the ambiguity of the Viking observational coverage. However, this year may have also been different, given the occurrence of the 1977b planet-encircling dust storm which occurred the preceding winter. At any rate there were few clouds detected in our processing in the southern hemisphere during mid-spring, due to the 1977b dust storm.

4.3.3. Interannual Variability: Viking Year 1 vs. Year 2

The greatest overlap occurs for the northern summer period, but even then there are considerable differences in the latitude-longitude coverage. Results are qualitatively similar. While both seasons indicate a cloudy zone in northern low latitudes, that zone appears even more pronounced and longitudinally extended in year 2. Clancy *et al.* [1996]

also reported a cloud band in northern mid-spring ($L_s \sim 65$) between 10S and 30N, observed in 1995 HST violet images.

4.3.4. Clouds associated with Topography

Slipher [1962] first observed clouds over the Tharsis plateau and the major volcanoes there in 1907. In his work, Slipher also discussed discrete “blue” clouds which had been seen frequently over time. Hartmann [1978] showed that most of the historical discrete blue clouds were condensate clouds associated with major volcanoes and other orographic uplift regions, which were, prior to Mariner 9, unknown to be topographic highs. Sixty percent of the blue clouds he studied (77 total) were associated with one of the following volcanoes: Olympus Mons, Ascraeus Mons, Pavonis Mons, Arsia Mons, Tharsis Tholus, Alba Mons, and Elysium Mons. Olympus Mons (called Nix Olympica), Arsia Mons (called South Spot), and Elysium Mons clouds were also seen in the Mariner 9 television experiment images [Leovy *et al.*, 1972]. We have identified clouds in our data in each of these regions except Tharsis Tholus, which is probably due to the lower resolution of our data.

Smith and Smith [1972] studied three topographic extremes on Mars: Hellas basin, Olympus Mons (called Nix Olympica in their paper), and Elysium Mons. They found the cloudiest season to be $L_s = 60-170$ (peaking between $L_s = 90-130$) over these areas. This is roughly consistent with our work, in which the cloudiest time period was $L_s = 60-140$. They thought the Hellas clouds were due to CO_2 frost formation, but we see a water ice cloud over Hellas in the $L_s = 110$ and $L_s = 125$ bins. In general, we saw clouds in the locations and during the seasons as did Smith and Smith [1972]. Their data were taken in 5 different years during opposition, coupling seasonal and interannual differences, whereas our data were taken over only 2 different Mars years.

James *et al.* [1996] saw discrete clouds associated with the Tharsis volcanos which were superimposed on the cloud band between -10S and 30N latitude, discussed above. During this same season, in addition to the similar cloud band, Olympus Mons and Pavonis Mons exhibited greater temperature differences. In HST images from 1991 near $L_s=60$, James *et al.* [1994] also saw discrete clouds over the Tharsis volcanoes, Elysium Mons, and over Arabia. In our data, clouds over the Tharsis volcanos were present from at least $L_s=60$ through the $L_s=125$ bin, whereas Elysium and Arabia also had widespread clouds for a similar season (our $L_s=65$ bin). In our $L_s=50$ bin, we saw Elysium and Arabia, but not much over Tharsis. Earlier in the northern spring, at $L_s=20$, Tharsis volcano clouds were also seen [James *et al.*, 1996]. However, discrete clouds associated with the Tharsis volcanos in our $L_s=20$ bin were not obvious, despite the good data coverage.

4.3.5. Hazes

French *et al.* [1981] and Kahn [1984] have previously mapped cloud distributions during the Mariner 9 and Viking period using the imaging systems aboard. These camera's higher resolution allowed identification of discrete clouds, for example over the Tharsis volcanoes, and other phenomena such as lee waves. Typically, the IRTM instruments did not have resolution to be able to see these types of clouds, unless their extent was quite large (e.g., Tharsis volcanos). Thus, IRTM was likely to see the more extended clouds which Kahn mapped as hazes. Kahn could not positively distinguish between water ice and dust hazes and classified both as "hazes." The restriction to mid-day times in our analysis also complicates comparison of the two data sets, especially for hazes, as they may occur more frequently at cooler times of day. Also, although the IRTM and Viking Imaging System (VIS) instruments were bore-sighted, their coverages are not identical as they frequently observed at different times (different parts of the orbit).

Our cloud maps show the lack of coverage as a function of season as black. Kahn showed coverage for the entire data set, but his latitude vs. season plots do not explicitly show lack of coverage. Finally, Kahn binned data from different Mars years together, whereas ours are separated, and he used $L_s=35^\circ-45^\circ$ seasonal bin sizes compared to our $L_s=15^\circ$ bin size.

Qualitatively, we see an increase in the northern low latitude cloudiness during the northern late spring and early summer, as did Kahn. There are some regions in which both data sets show clouds at the same seasons, in particular, over Tharsis. However, there are cases in which one data set will show clouds, but the other will not. For instance, we show a strong and widespread signature over the Hellas basin in the early northern summer, yet Kahn maps only a few thick haze points in this region. We also show a widespread yet weaker signature over Alba Patera in mid-northern spring, which does not appear in Kahn's maps. Conversely, Kahn sees hazes over Hellas in the early-mid spring and we do not. Such differences may reflect the fact that our IR cloud signature requires strong thermal contrast whereas Kahn's haze detection depends on albedo differences: these differences are not necessarily correlated. Interestingly, in the early northern spring, both data sets show an absence of low-latitude signatures and similarly, both data sets show a drop off in signature in the equatorial region in the late northern fall. Finally, the locations of our strongest signatures do not always correspond to Kahn's moderate/thick hazes indicating that our cloud signatures may result from a greater cloud to surface temperature contrast rather than a higher opacity cloud.

5. Conclusions

The techniques developed and employed here have allowed water-ice clouds to be identified in the Viking IRTM data set with greater confidence than in previous work. The maps presented here provide improved longitudinal, latitudinal and seasonal variation

of the occurrence of water-ice clouds for the Viking period. While even better space-time coverage will be provided by the ongoing Mars Global Surveyor and the upcoming Mars Climate Orbiter missions, the clouds identified in the Viking data set provide an important reference for the study of the Mars water cycle and its interannual variation. In particular, the cloud maps derived here indicate that there were extensive water-ice clouds during the Viking period, comparable to that suggested by more recent HST monitoring of Mars, even given the presence of a significant amount of atmospheric dust during the period of Viking observations.

Key to the detection of water ice clouds in the IRTM data set is the treatment of the variable surface emissivity. The scheme developed and applied here, which used the emissivities derived by Christensen [1998], enabled confident detection of the thermal infrared signature of water-ice clouds against a heterogeneous background. Ignoring these surface effects would have produced a large number of false “cloud” detections. Furthermore, the main source of uncertainty in the present detection scheme (outside of dust storm periods) is due to the remaining imprecision in the surface emissivity determination.

In the cloud maps derived here, the best evidence for a cloudy zone due to the rising branch of the Mars Hadley circulation is the development of a cloud band centered near 45S in late northern winter, followed by the disappearance of low latitude clouds and cloud bands in early spring ($L_s=20$), and the emergence of a cloudy zone in northern low latitudes during northern mid-spring. No similar transition was seen during the northern fall equinox, possibly because of the effects of two major dust storms (and the difficulty of detecting water-ice clouds during such events with the present detection scheme). The northern winter/spring reversal occurred in the period $L_s=20-50$, consistent with Mariner 9 observations, but later than models have been predicting.

Polar hood and storm system clouds are not well resolved with the IRTM temporal coverage and our restriction to nonpolar latitudes. There was some evidence for extension

of the north polar hood into northern middle latitudes and for the presence of northern storm tracks, the latter occurring most frequently and appearing to penetrate farthest toward the equator in the Acidalia Planitia longitudinal sector. Similar excursions of the south polar hood were not observed following the very dusty spring and summer observed by Viking.

There was little evidence for substantial interannual variability between the two successive northern summers observed by the Viking Orbiters. Furthermore, some features seen in northern spring and summer are qualitatively similar to cloud observations by HST in years since the Viking mission ended.

Consistent with observations back as far as 1907 [*Slipher, 1962, Leovy et al., 1972, Smith and Smith, 1972, Hartmann, 1978, James et al., 1994*], we saw discrete water ice clouds over many topographic highs including, Olympus Mons, Pavonis Mons, Arsia Mons, Ascraeus Mons, Elysium Mons, and Alba Patera. These clouds were often seen in the same season as previous observations [*Smith and Smith, 1972, James et al., 1994*]. Discrete clouds were also identified in our data even when superimposed on a background cloud band as in *James et al. [1996]*. We saw a strong water ice cloud signature over Hellas basin. *Smith and Smith [1972]* also saw a bright, large cloud at this seasons, but identified it as CO₂ frost, not being associated with a topographic high.

While the data presented here only represent only a part of the entire Viking IRTM data set, the detection of clouds at night and near the terminators will be difficult using the IRTM data set because of the lack of adequate constraints on the temperature profile and the expected lower surface-cloud temperature contrast. The best opportunity perhaps would be provided by the predawn observations when the surface is coldest. Determining physical properties (opacity and particle size) is also limited by the lack of independent dust and temperature profile constraints. These cloud properties are best determined using some of the stronger cloud signatures identified here.

The cloud maps derived here should provide a valuable comparison with GCM vertical velocity fields and, of course, with ongoing observations by the Mars Global Surveyor TES [*Christensen et al.*, 1992] and, later, to data from the Mars Climate Orbiter (MCO) Pressure Modulator Infrared Radiometer [PMIRR, *McCleese et al.*, 1992] data. With TES and PMIRR nadir data, an analysis similar to the one used here can be performed, although PMIRR will have less thermal contrast between the surface and atmosphere in its late afternoon orbit (2 p.m. for MGS; 4 p.m. for MCO). Detecting clouds with these observations will require, of course, proper attention to the effect of the variable surface emissivity, as discussed here. Limb views by TES and PMIRR (the latter with its smaller field of view) will be less sensitive to the surface emissivity effects dealt with here and will directly provide cloud altitudes. The major advantage of the MGS and MCO observations is the daily global coverage achieved by each spacecraft, albeit at just two times of day. Other advantages over Viking IRTM come from the ability of TES and PMIRR to simultaneously retrieve temperature and aerosol extinction. That should permit a more direct estimate of cloud opacity and the interactions between dust and ice suspended in the Mars atmosphere, as evidenced by their spatial variations.

List of Figures

Figure 1. Viking orbiter IRTM spectra. (a) A typical spectrum of Mars with no atmospheric water ice or dust contamination. The strong absorption at 667 cm^{-1} is due to the vibrational band of gaseous CO_2 in the Martian atmosphere. (b) A spectrum showing a dust cloud absorption centered near 1100 cm^{-1} ($9\text{ }\mu\text{m}$) and (c) a spectrum showing a water ice cloud absorption (shoulder near $800\text{-}900\text{ cm}^{-1}$). (d) A theoretical model for a water ice cloud in the Martian atmosphere [Curran *et al.*, 1973]. (e) The IRTM band passes, labelled above with their μm designation. The x-axis is wavenumber (cm^{-1}) and the y-axis shows different brightness temperatures scales (K) for the different spectra.

Figure 2. Path A is a diagram of the surface spectral emissivity determination process [Christensen, 1998]. Path B shows how those values are used in the modelled brightness temperature determination. T_λ = wavelength dependent brightness temperature; T_{λ^*} = highest brightness temperature measured for given position; λ^* = wavelength associated with highest brightness temperature measured; T_k^{NC} = derived surface kinetic temperature; ϵ_λ = wavelength dependent surface emissivity; $R_\lambda(T_\lambda)$ = radiance of given temperature; I_s = thermal inertia of the surface [Pleskot and Miner, 1981]; A_s = albedo of the surface [Palluconi and Kieffer, 1981], T_{20}^{NC} = $20\text{ }\mu\text{m}$ modelled temperature with no clouds (dust or water ice) present; W_{20} = $20\text{ }\mu\text{m}$ weighting function; R_{20}^{NC} = radiance at $20\text{ }\mu\text{m}$ with no clouds present; T_k^{NC} = derived kinetic brightness temperature of the surface with no

clouds present; W_λ , R_λ^{NC} , T_λ^{NC} = weighting functions, radiances, brightness temperatures for other IRTM band passes; $R_{\lambda_k}^{\text{NC}}$ = radiance of derived kinetic brightness temperature of surface with no clouds present; ΔT_s^{NC} = difference in brightness temperatures resulting from surface emissivity effects alone; $\Delta T_{(C+S)}$ = difference in measured brightness temperatures (includes any atmospheric clouds - dust or water ice, depending on channels being compared - and surface emissivity effects); Δ_w = residual water ice cloud signature; Δ_D = residual dust cloud signature; β = threshold for identification of water ice clouds.

Figure 3. (a) Original T_{11} - T_{20} map without surface emissivity removed ($\Delta T_{(C+S)}$), (b) modelled T_{11} - T_{20} map (ΔT_s^{NC}), and (c) residual T_{11} - T_{20} map ($\Delta_w = \Delta T_{(C+S)} - \Delta T_s^{\text{NC}}$). Note features such as Sirtis Major and Acidalia Planitia in (a) and (b) and their disappearance in (c).

Figure 4. Water ice and dust clouds were modelled at a variety of cloud temperatures and cloud opacities for two dust compositions (see text). Water ice (+) and dust (\diamond , Δ , \square , \times) are plotted for different surface emissivity cases (see Table 1 and text). Case 1 shows (a) palagonite and (b) montmorillonite+basalt in which representative ϵ_λ values were separated by not only the difference in their means, but separated further by 1- σ on each value (e.g., text Eq. 2). Case 2 shows (c) palagonite and (d) montmorillonite+basalt in which representative ϵ_λ values were separated by only the difference in their means. The modelled dust with the lowest

Δ_w values are those with $\epsilon_{11} > \epsilon_{20}$. Case 1 uses $\epsilon_{11} - \epsilon_{20} > 0.0367$ and Case 2 uses $\epsilon_{11} - \epsilon_{20} > 0.0113$. Also shown is the $\Delta_w < -1.0$ K threshold used as an indicator of water ice clouds.

Figure 5. Surface plots showing which lat/lon bins contain (a) $\epsilon_{11} - \epsilon_{20} > 0$, (b) $\epsilon_{11} - \epsilon_{20} > 0.0113$, the difference between the mean ϵ_{11} and ϵ_{20} values, and (c) $\epsilon_{11} - \epsilon_{20} > 0.0367$, the case representing a difference of the mean plus $1-\sigma$. Note that the latter case only actually occurs in 5 data bins. Case (b) also occurs infrequently and does not resemble the cloud maps shown in Figure 9, indicating that we are not confusing dust with water ice clouds.

Figure 6. Residual water ice cloud maps using different Δ_w “threshold” criteria. In all cases, west longitude is shown on the x-axis, latitude on the y-axis, black indicates no data or data that didn’t meet the threshold, and the temperature scale ranges from -10 K (blue) to +10 K (red). (a) No threshold is used to isolate water ice clouds. (b) A strict threshold of $\Delta_w < -2.9$ K is used to isolate water ice clouds. (c) A relaxed threshold of $\Delta_w < -1.0$ K is used to isolate the water ice clouds.

Figure 7. The water ice cloud maps. The set covers $L_s = 80$ in Viking’s first year of taking data through $L_s = 185$ in Viking’s second year of taking data. Each map contains 15° of L_s with the beginning L_s labeled above. In all cases, west longitude is shown on the x-axis, latitude is shown on the y-axis, black indicates no $T_{11} - T_{20}$ data, white indicates bins which did not meet the $\Delta_w < -1.0$ K criterion, and the

clouds are shown in blues according to the temperature scale on the right which varies from -10 K (dark blue) to +10 K (red).

Figure 8. Clouds (solid line) and IRTM coverage (dashed line) as a function of season and latitude. $L_s=200-245$ and $L_s=275-335$ have been annotated with 1977a and 1977b indicating the first and second major dust storms, respectively, during the Viking mission. During the 4 seasonal bins of the 1977b dust storm, the dust opacity was high enough that they have been over-corrected in our surface emissivity removal process and therefore, the clouds shown should not be trusted.

Table 1. Water ice cloud and dust symbols used for different modelled emissivity cases. Note that the only cases in which dust could be confused with water ice clouds (\diamond and Δ) occur over surfaces with $\epsilon_{11} > \epsilon_{20}$.

Fig. 1

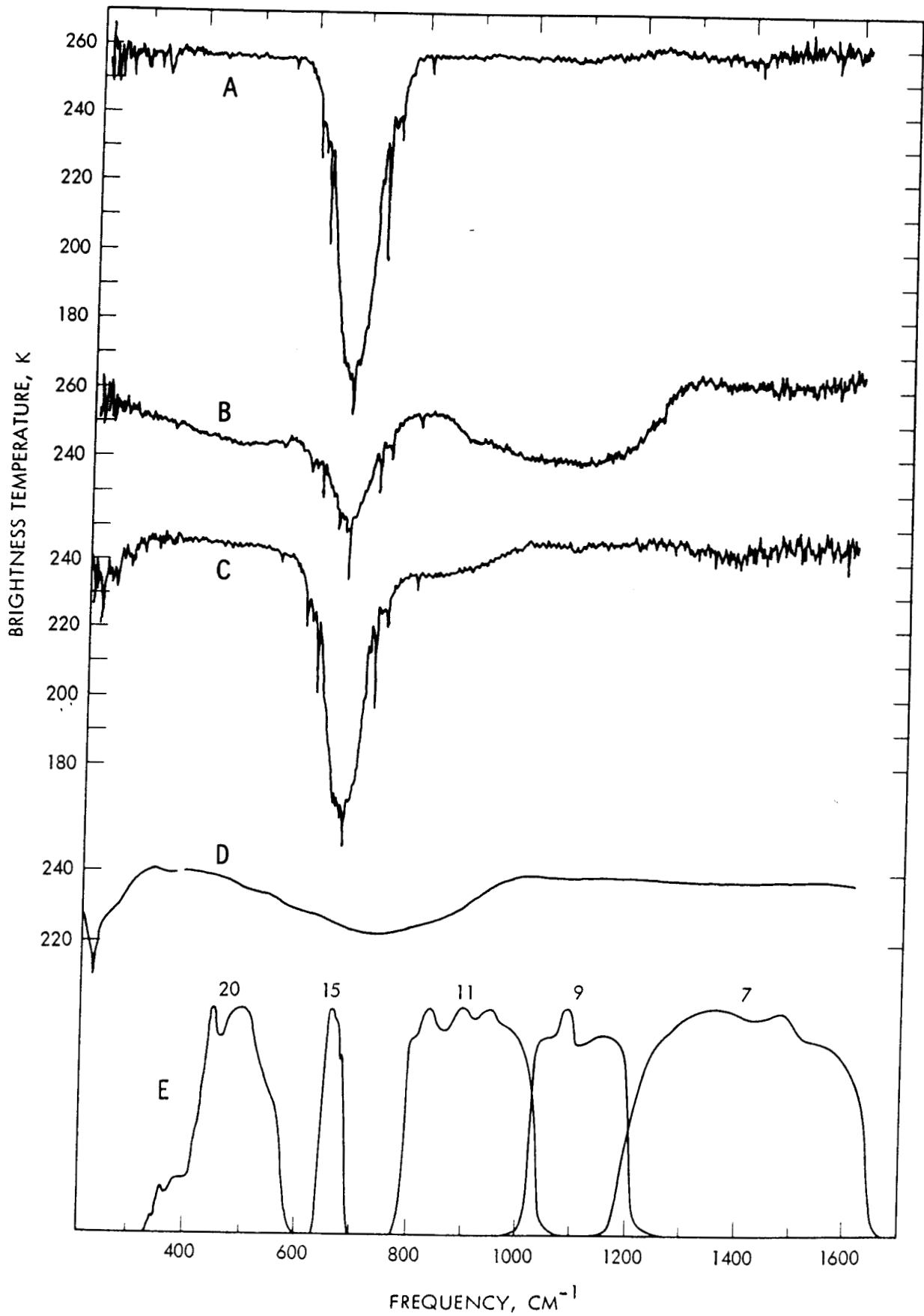
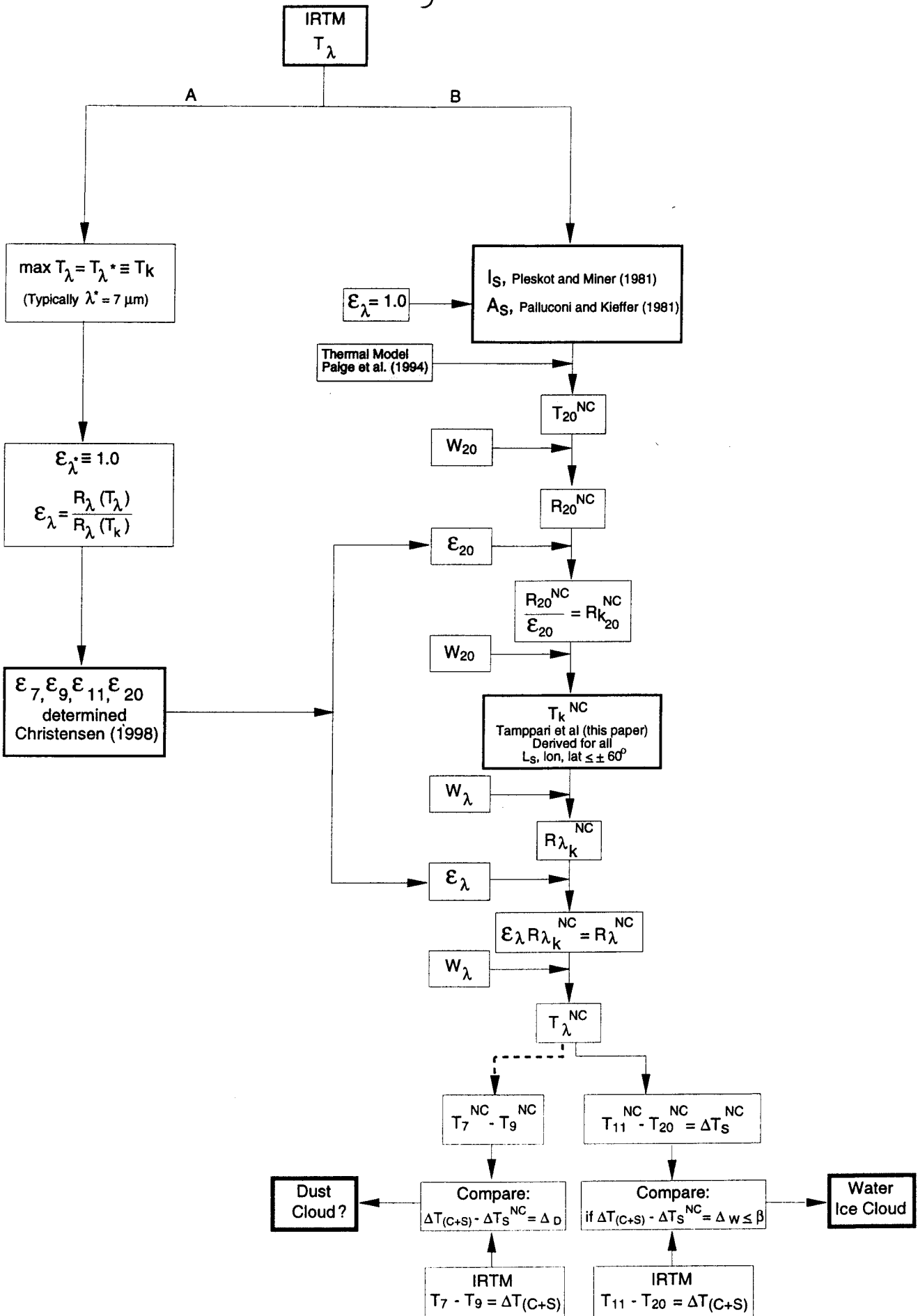


Fig. 2



Cloud free $T_\lambda (T_\lambda^{NC})$ generation

Cloud detection scheme

Fig. 3

Year One: $L_s = [20, 35]$

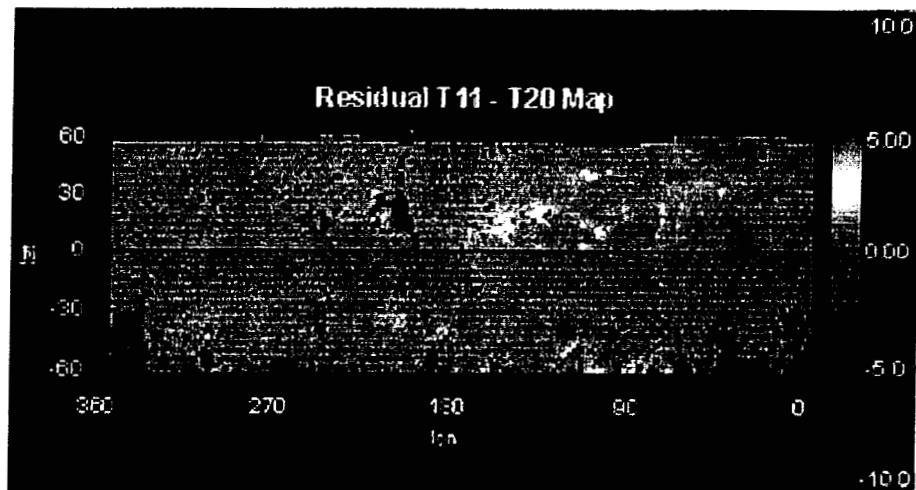
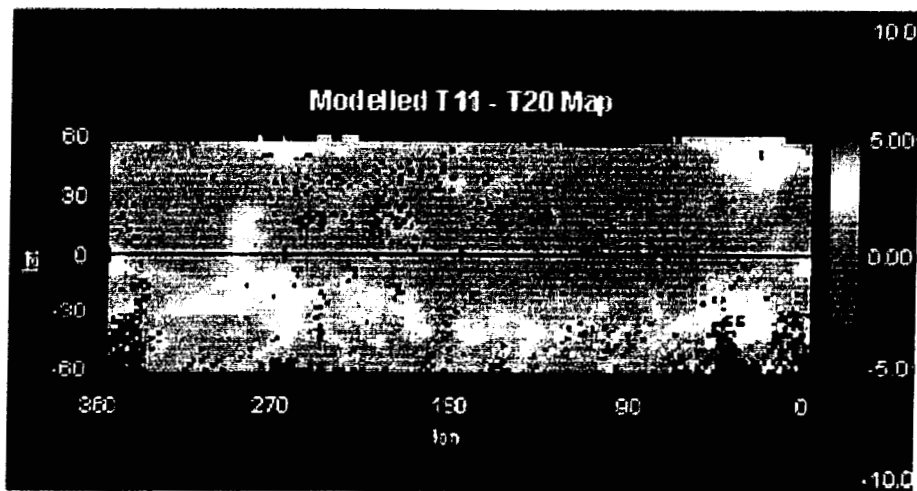
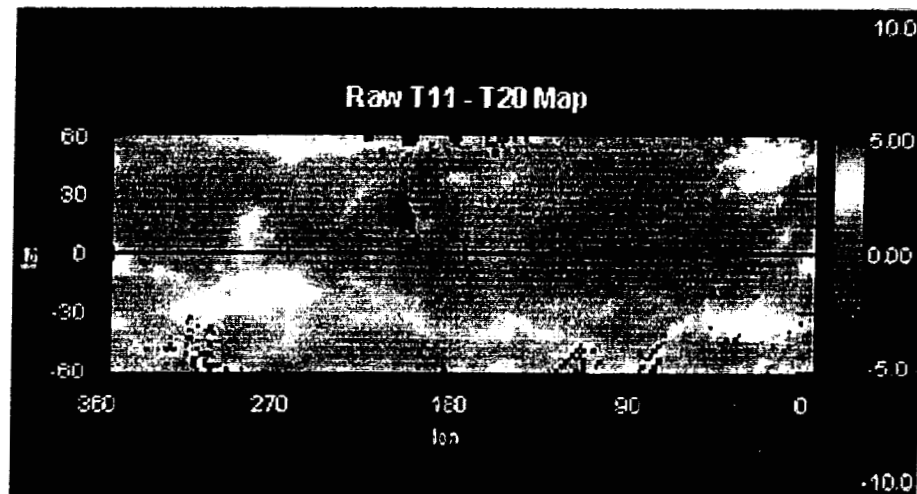


Fig. 4

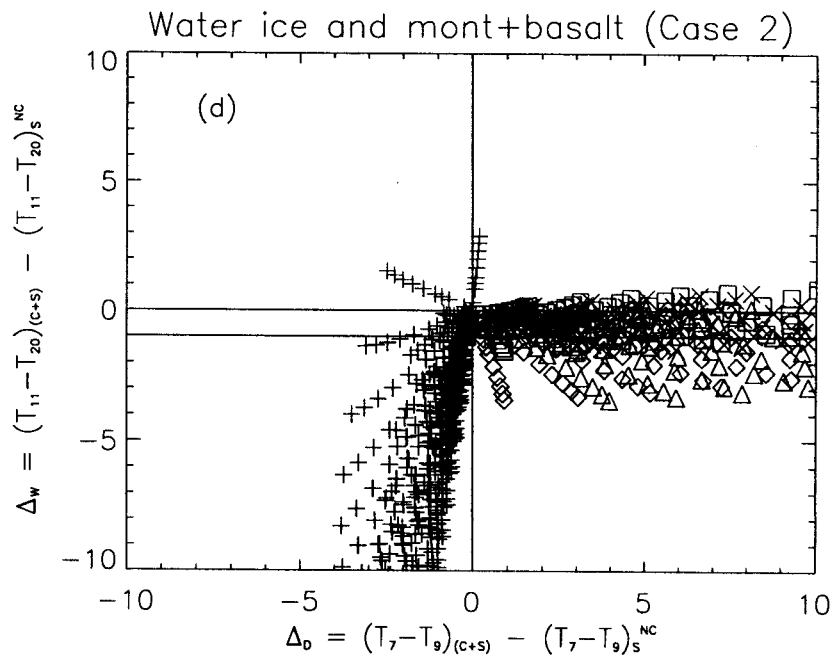
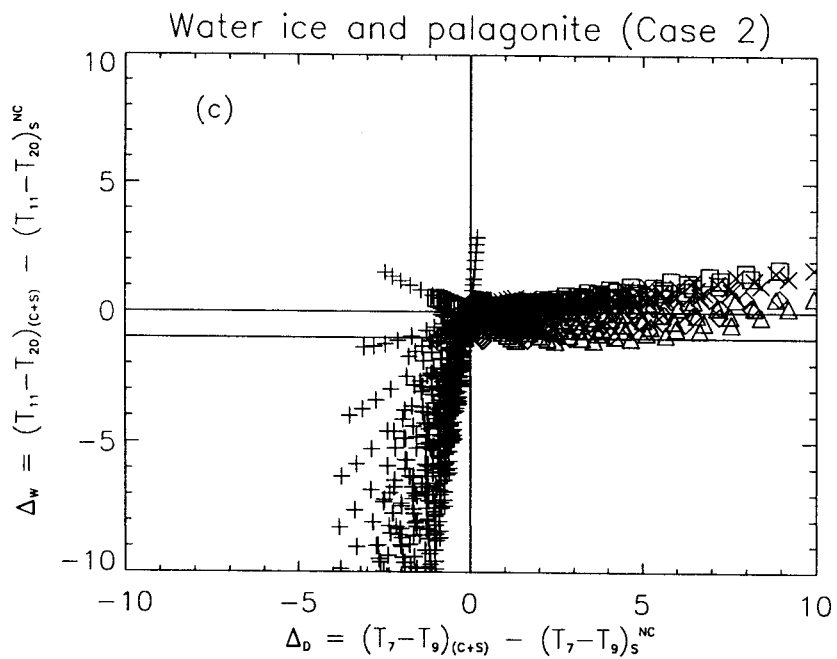
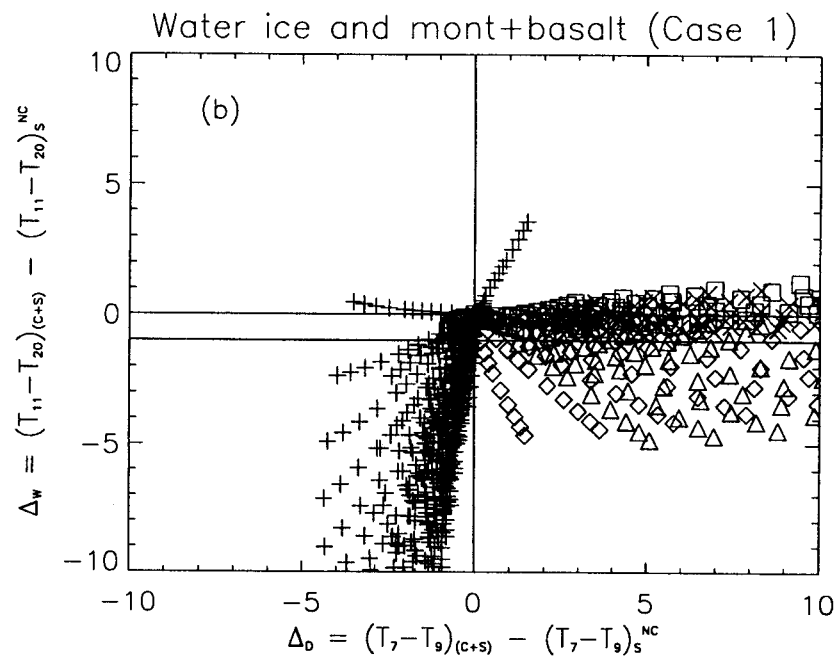
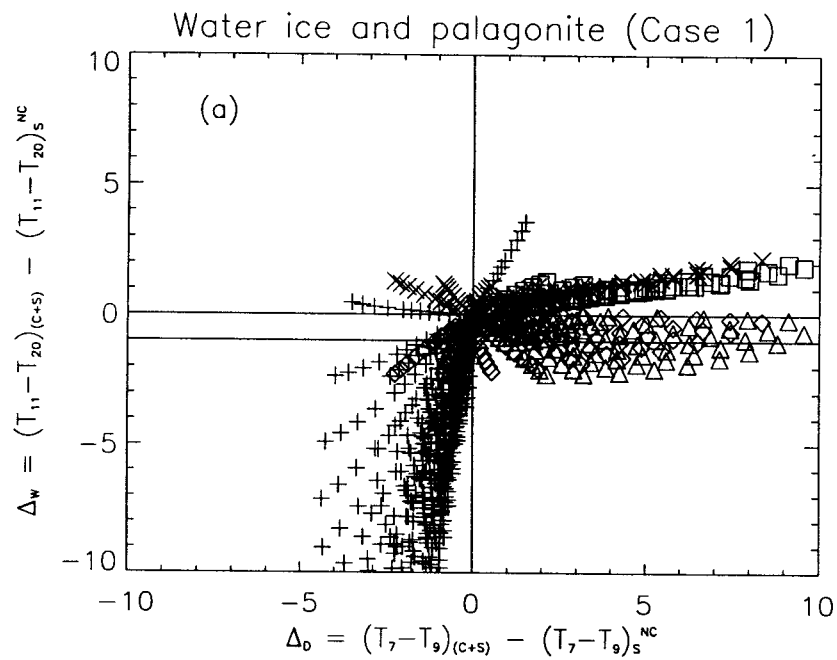


Fig. 5

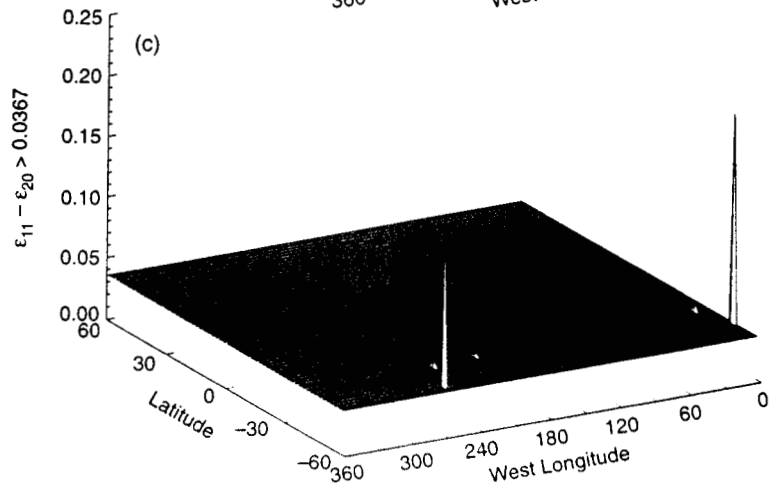
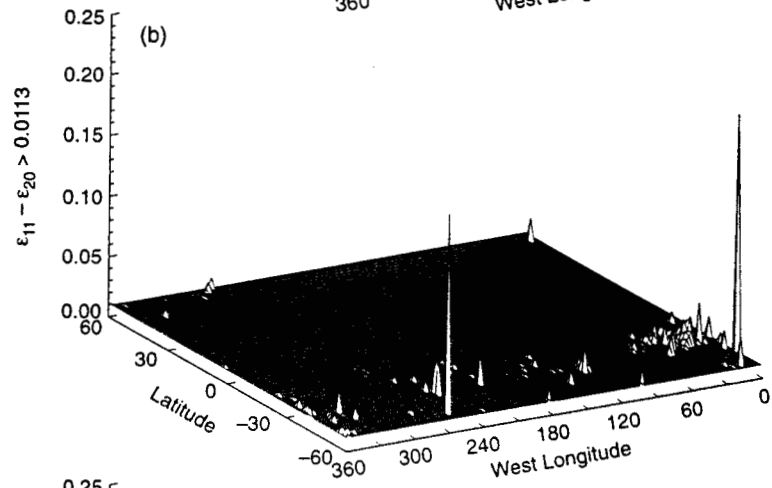
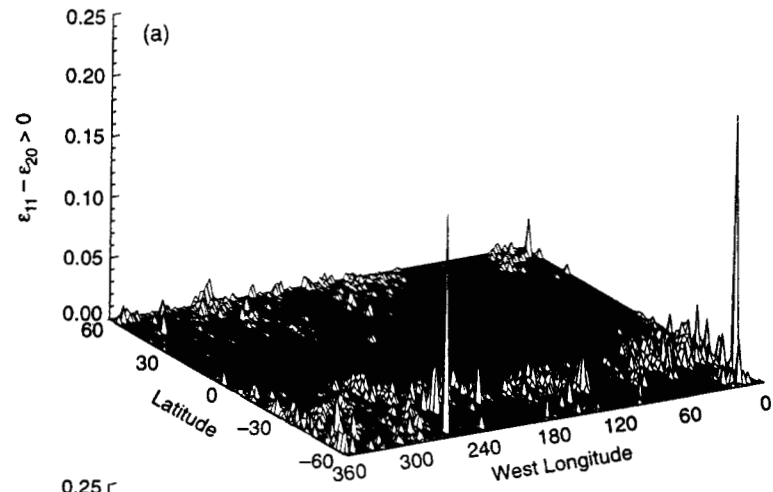
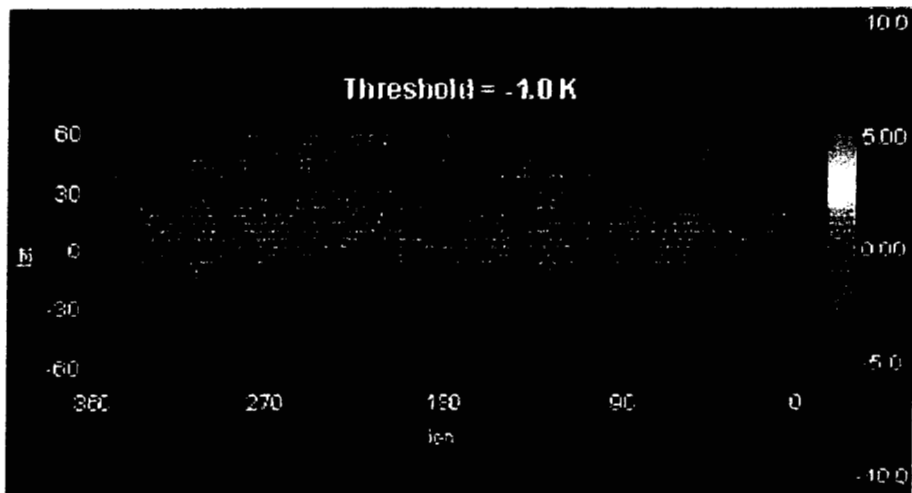
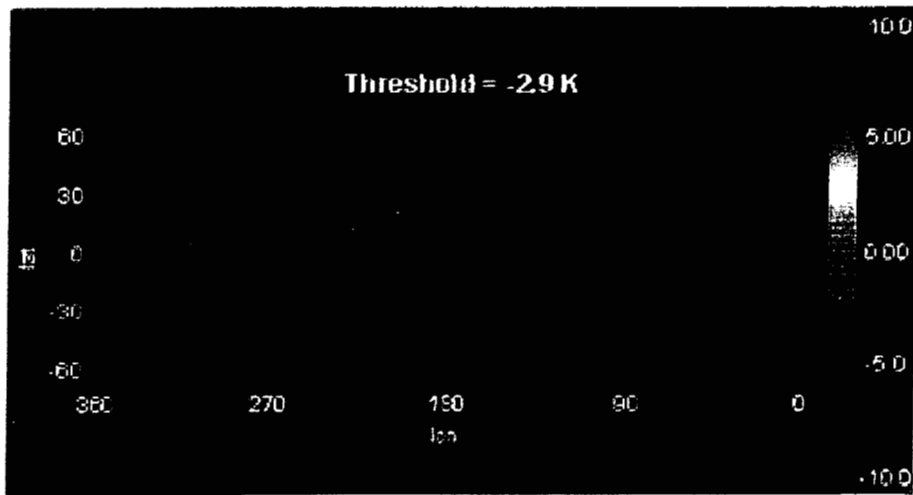
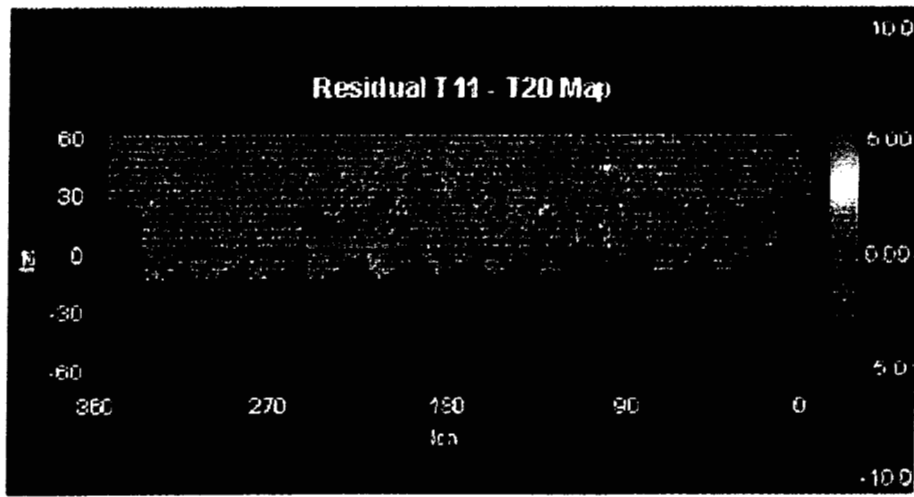


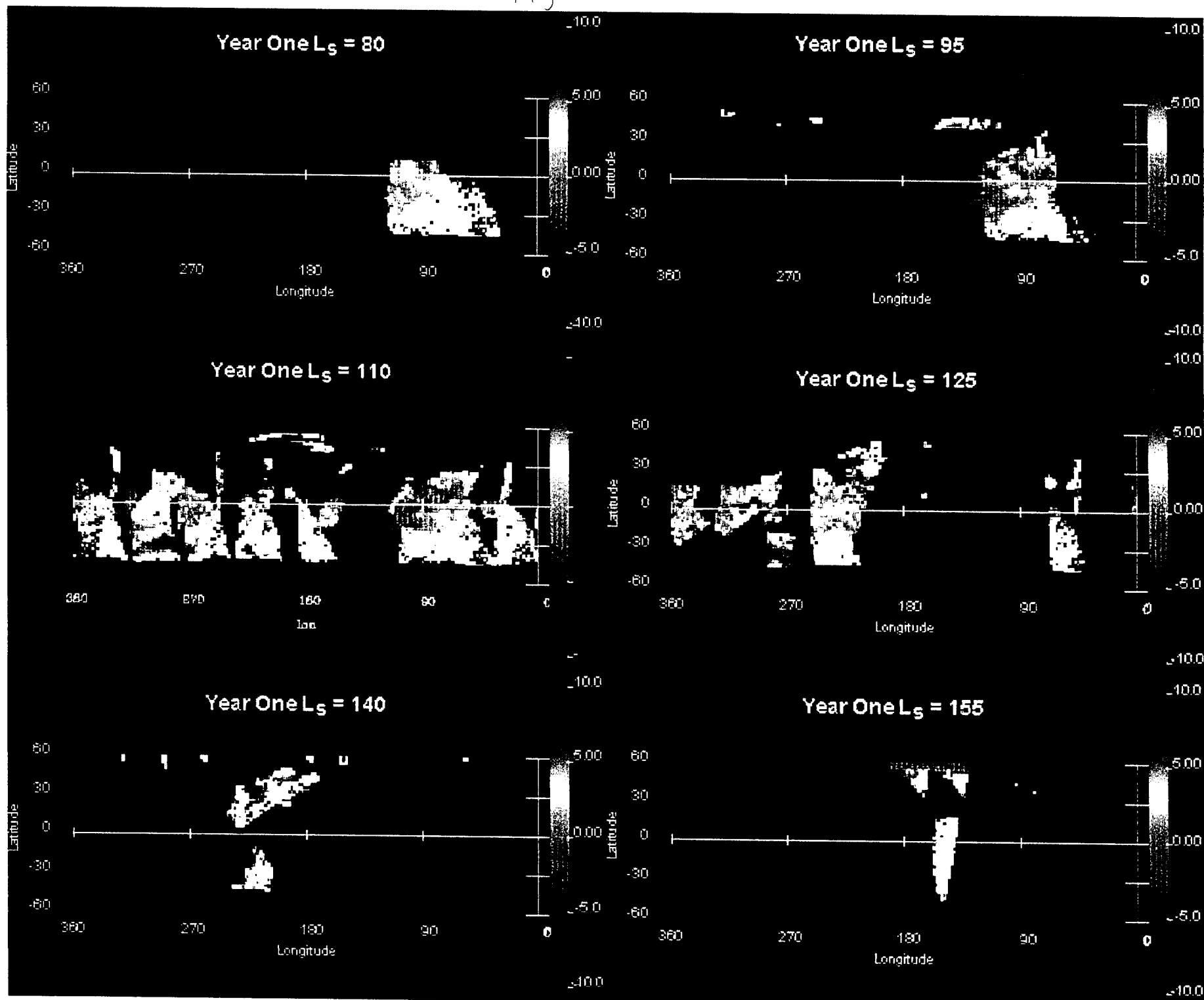
Fig. 6

Year Two: $L_S = [95, 110]$

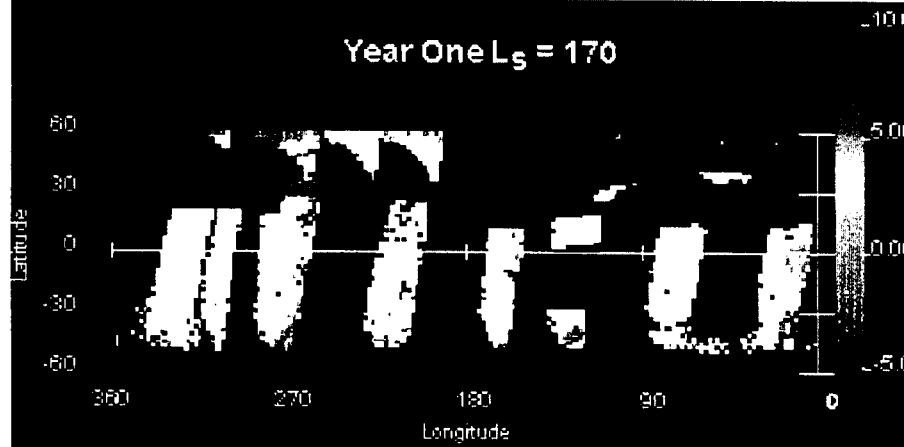


5. 5734

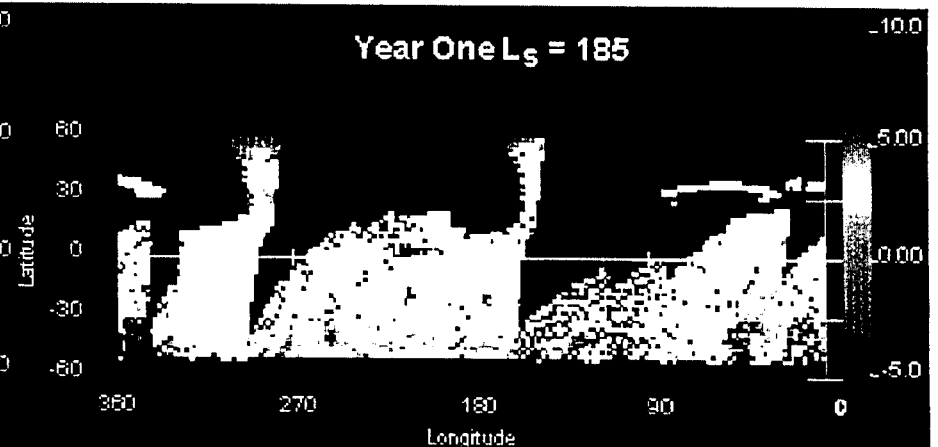




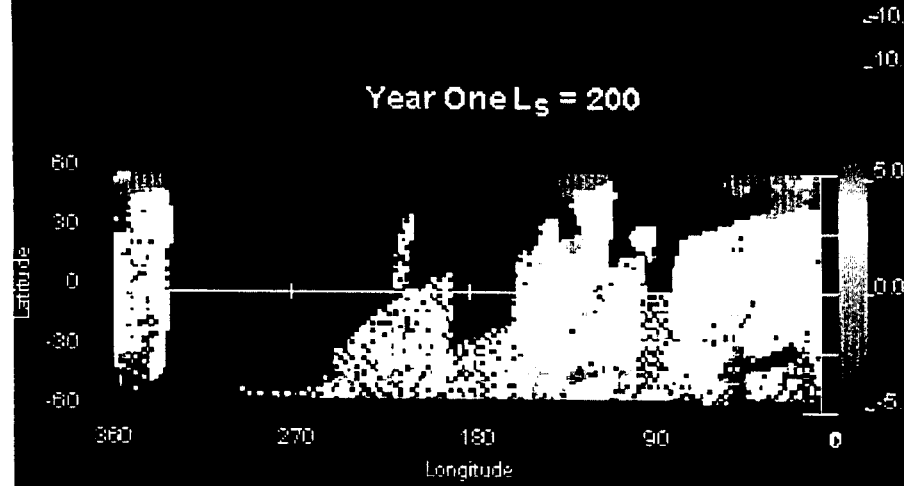
Year One $L_S = 170$



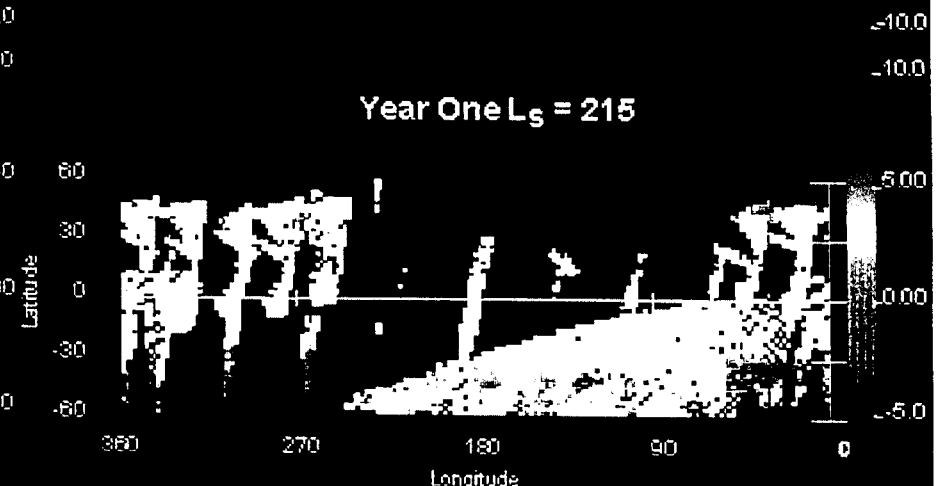
Year One $L_S = 185$



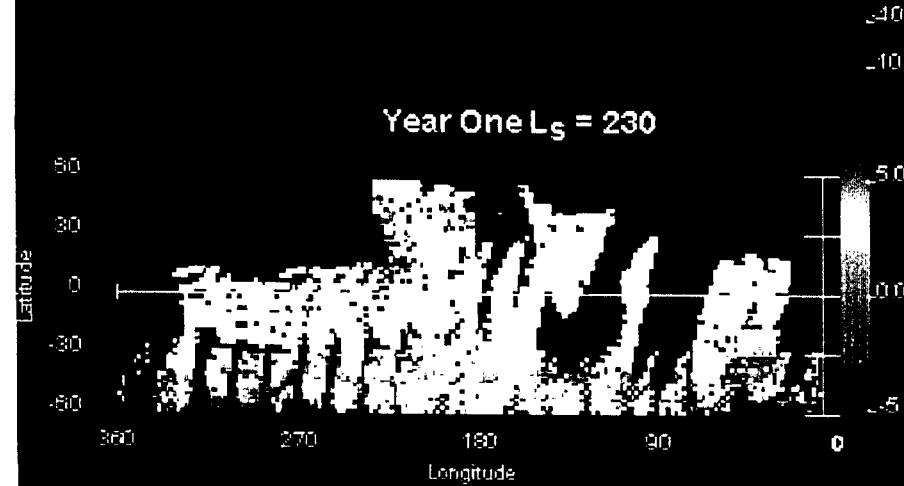
Year One $L_S = 200$



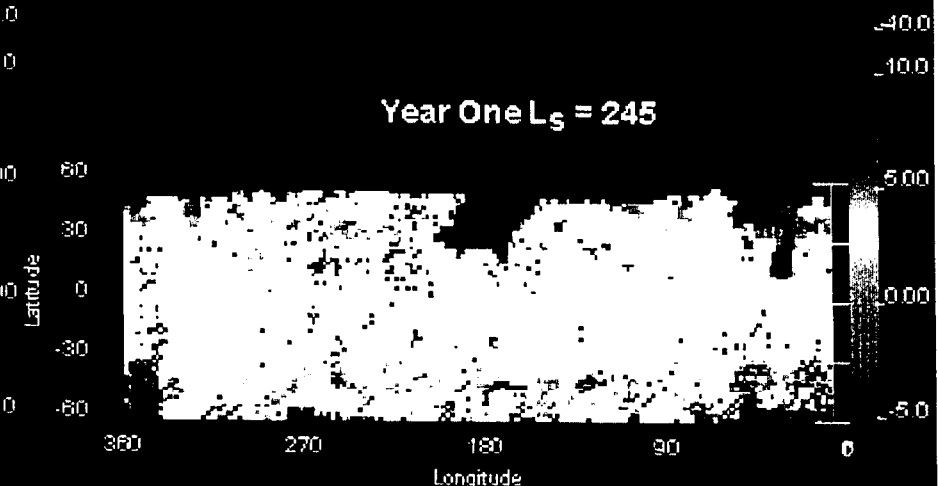
Year One $L_S = 215$



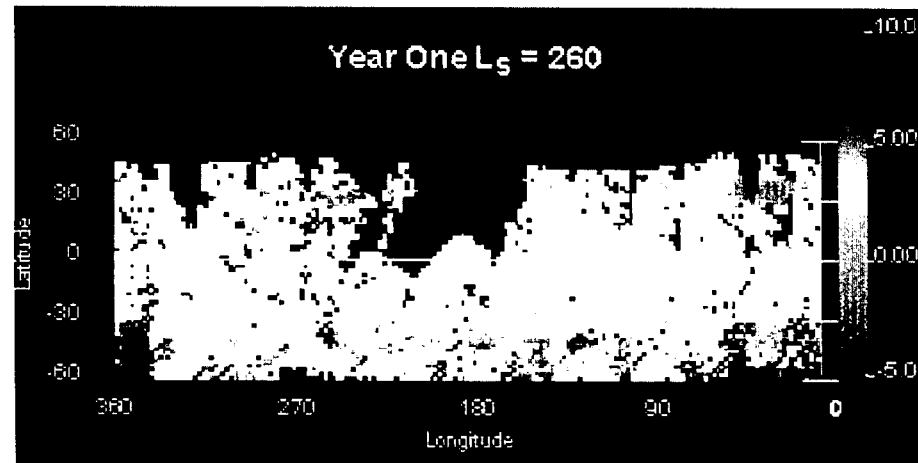
Year One $L_S = 230$



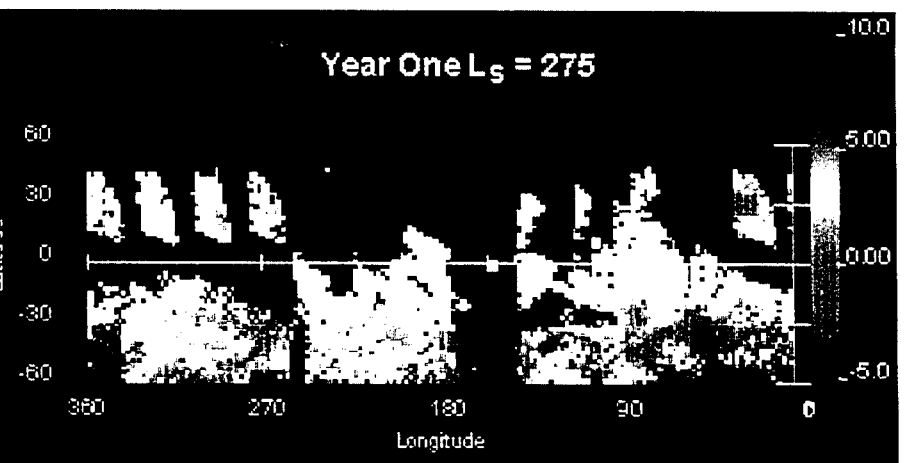
Year One $L_S = 245$



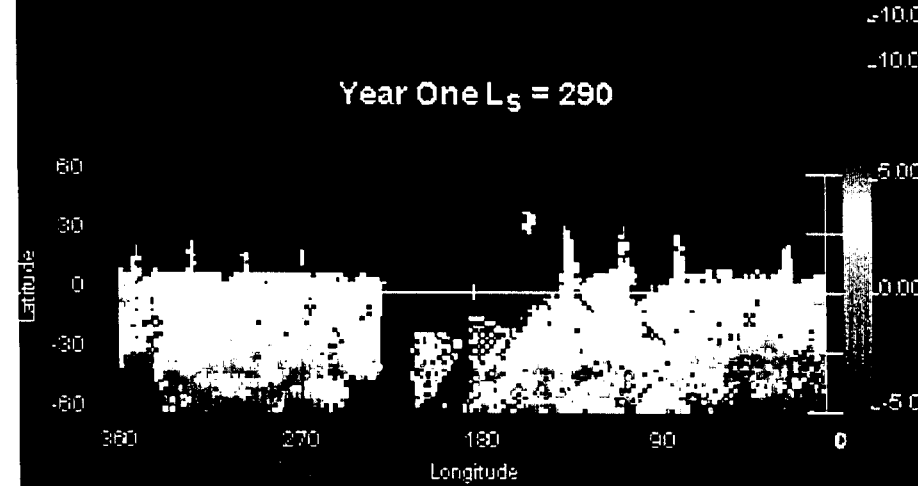
Year One $L_S = 260$



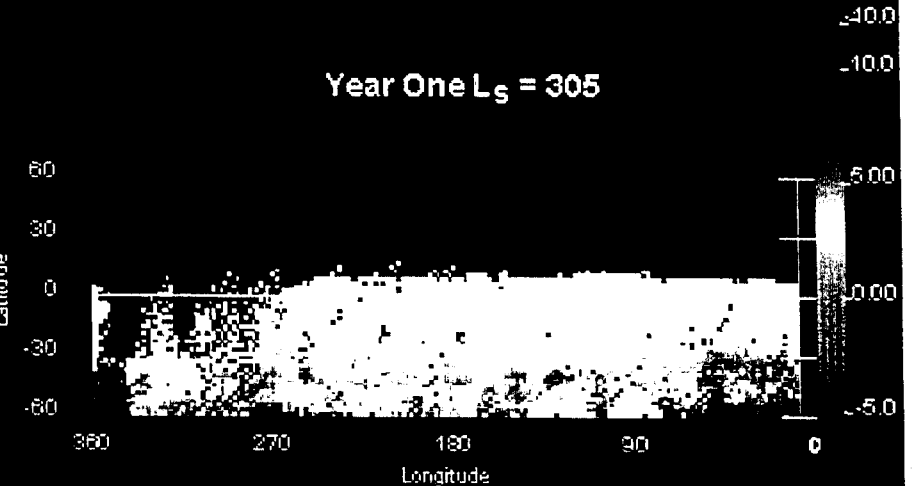
Year One $L_S = 275$



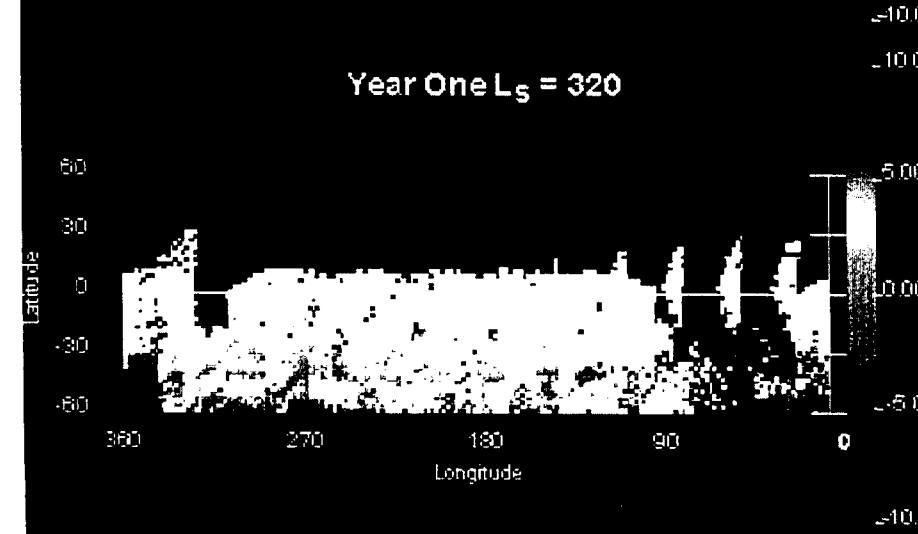
Year One $L_S = 290$



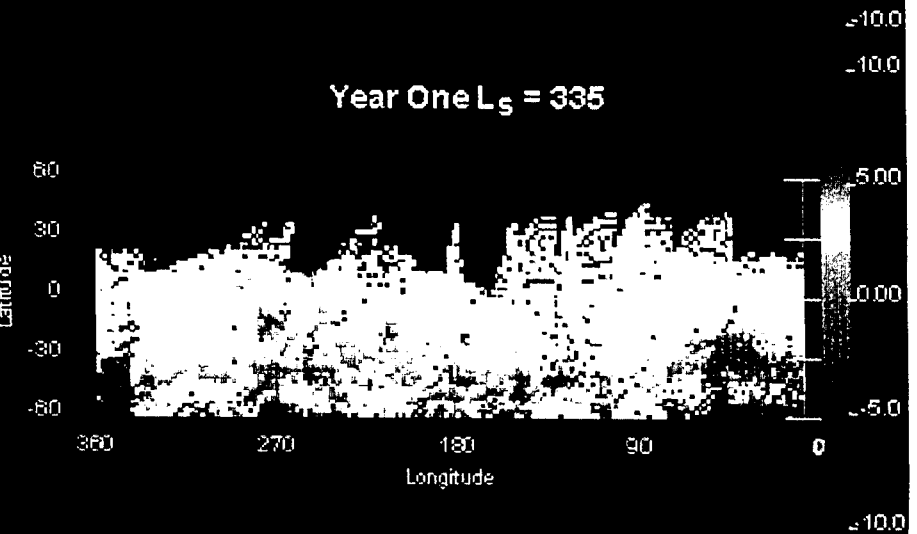
Year One $L_S = 305$



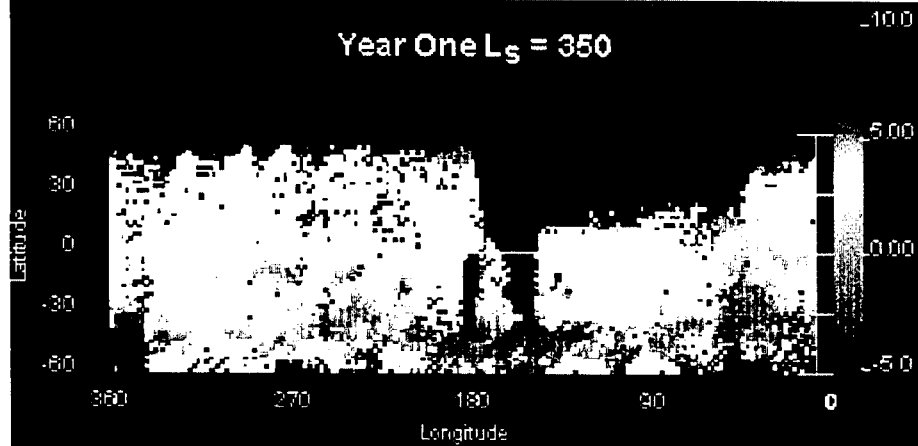
Year One $L_S = 320$



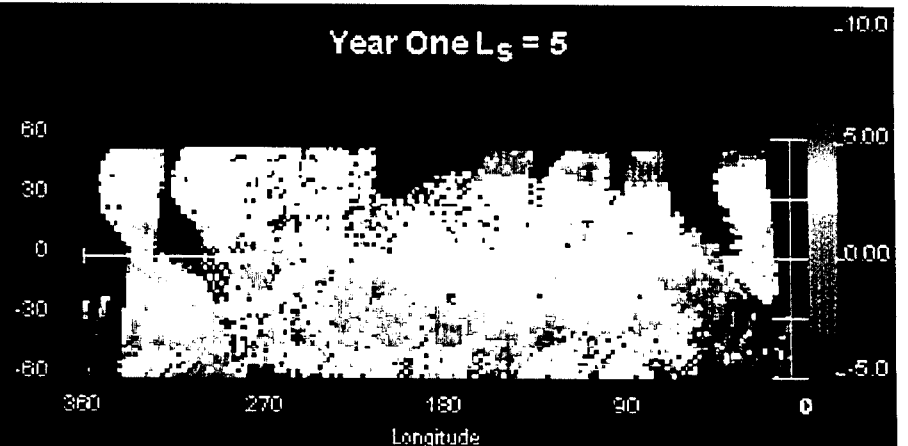
Year One $L_S = 335$



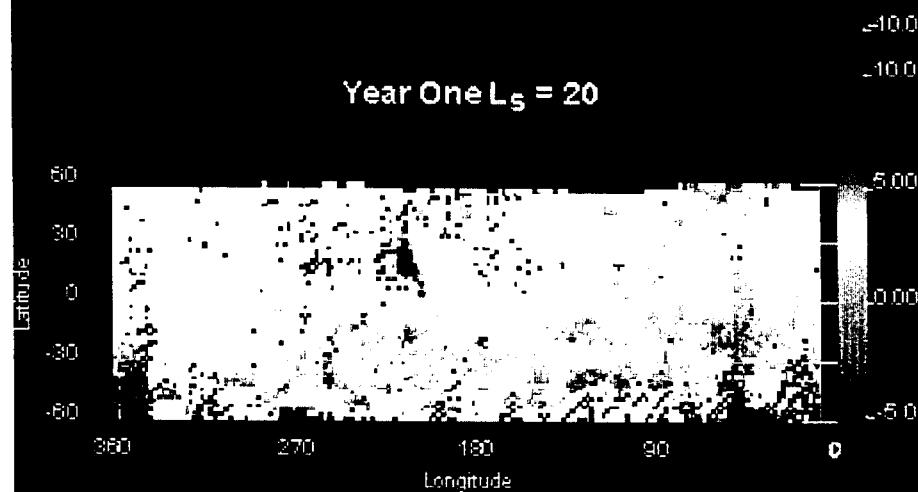
Year One $L_S = 350$



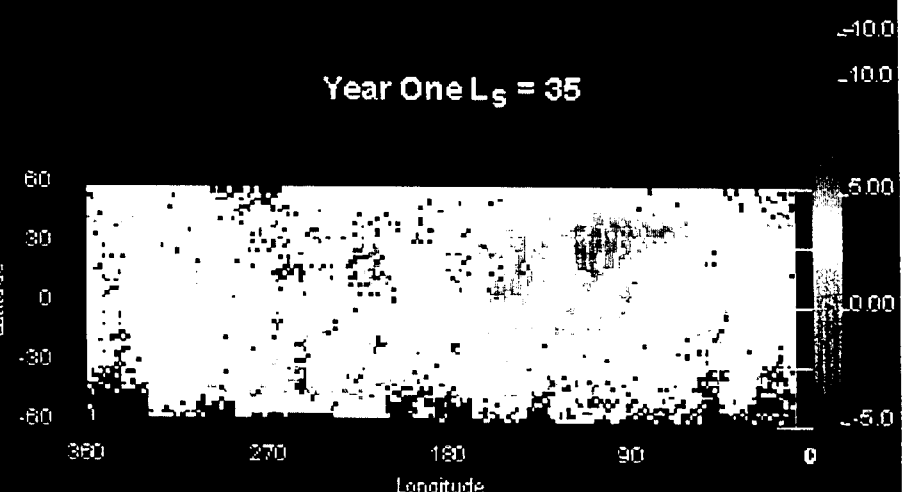
Year One $L_S = 5$



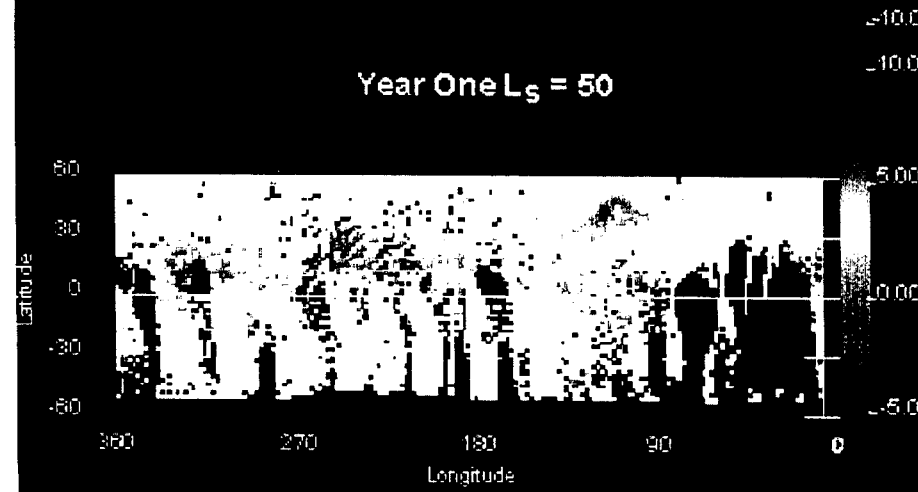
Year One $L_S = 20$



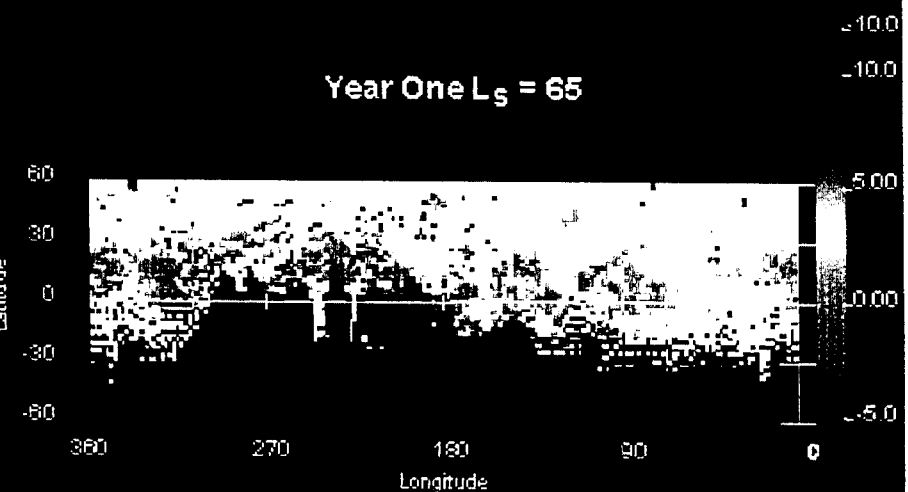
Year One $L_S = 35$



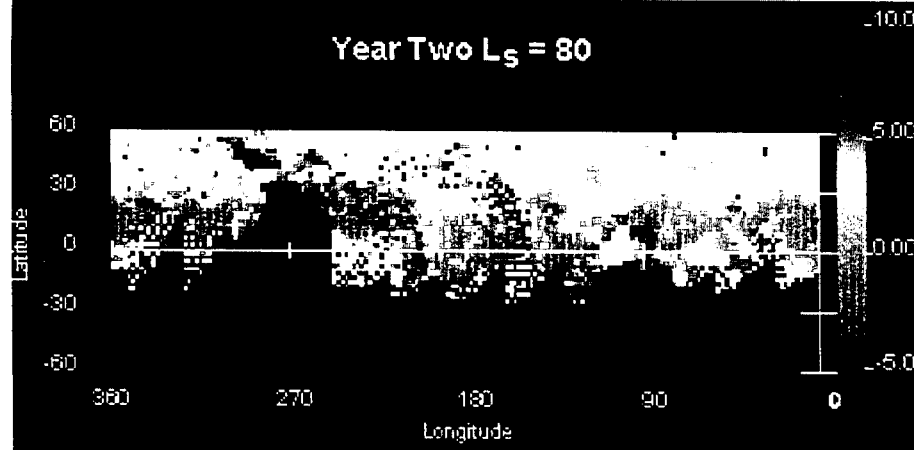
Year One $L_S = 50$



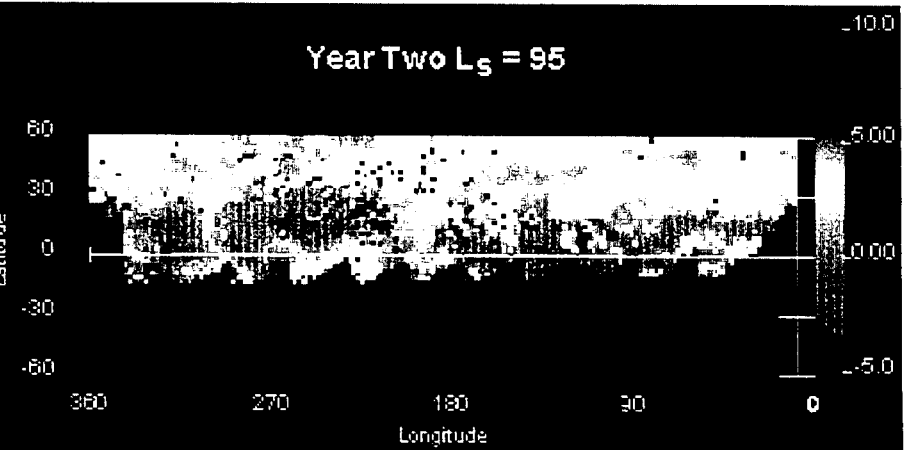
Year One $L_S = 65$



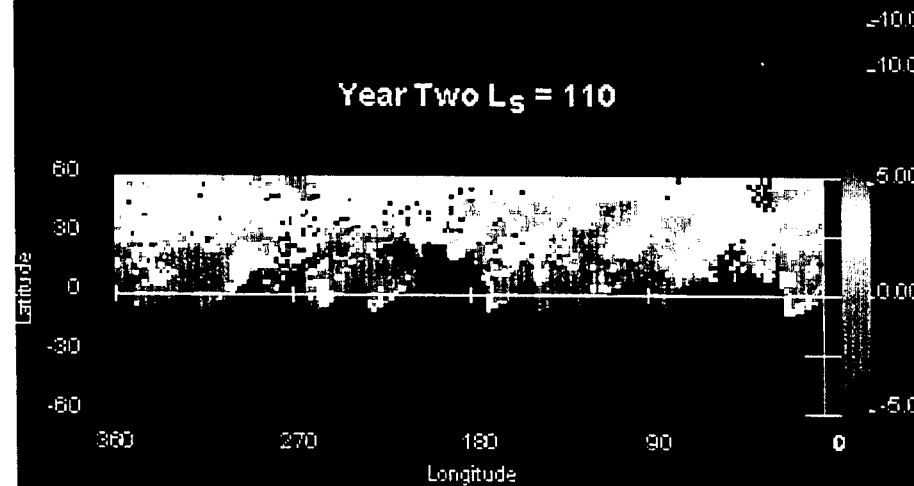
Year Two $L_S = 80$



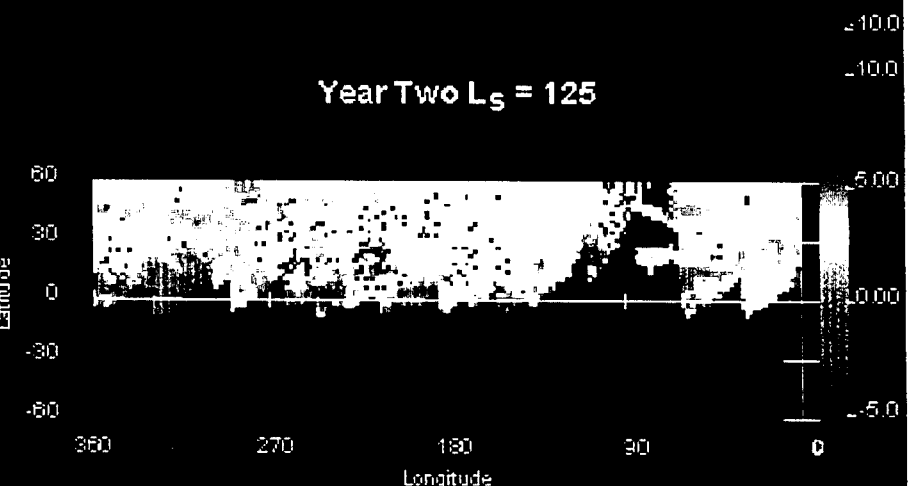
Year Two $L_S = 95$



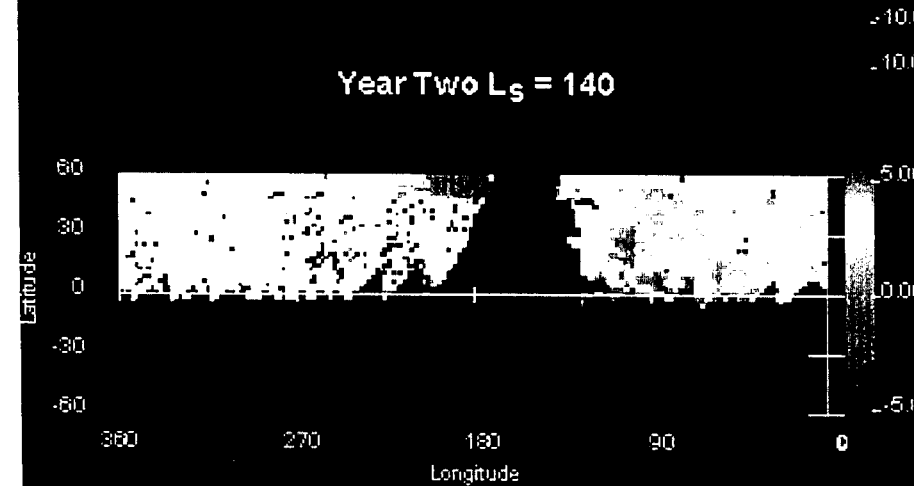
Year Two $L_S = 110$



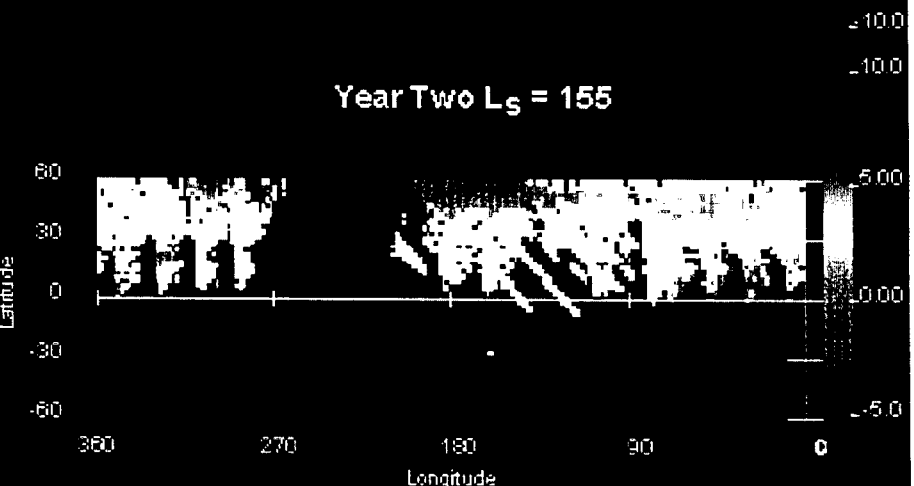
Year Two $L_S = 125$



Year Two $L_S = 140$



Year Two $L_S = 155$



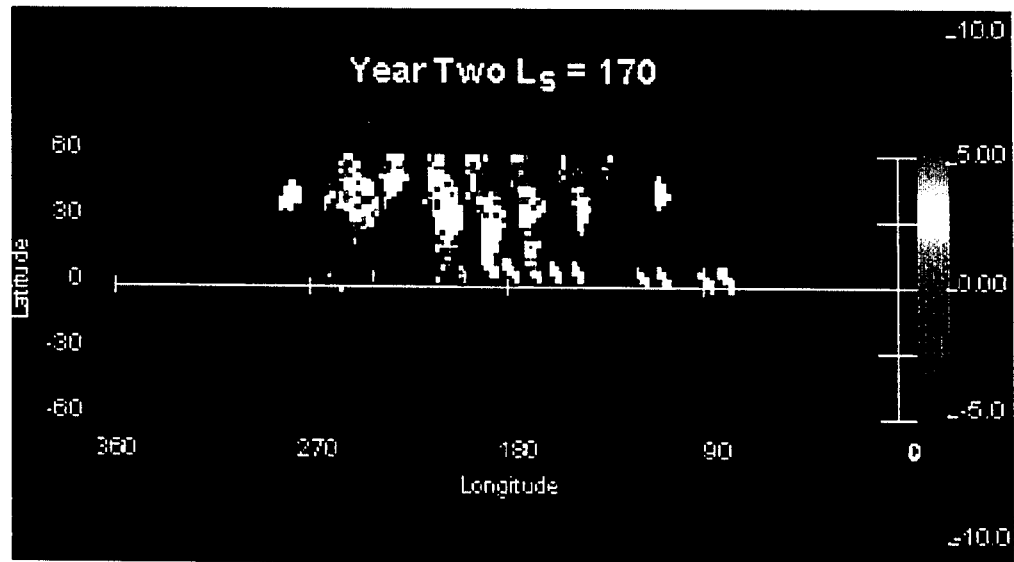


Table 1. Water ice cloud and dust symbols

Water ice symbol	Dust symbol	sign of $\epsilon_{11}-\epsilon_{20}$	sign of $\epsilon_7-\epsilon_9$
+	\diamond	>0	>0
+	Δ	>0	<0
+	\square	<0	<0
+	\times	<0	>0

Bibliography.

Barnes, J. R., Time spectral analysis of midlatitude disturbances in the Martian atmosphere. *J. Atmos. Sci.* 37, 2002-2015, 1980.

Briggs, G. A., C. B. Leovy, Mariner 9 observations of the Mars north polar hood, *Bull. Am. Meteor. Soc.*, 55 (4), pp. 278-296, 1974.

Briggs, G. A., W. A. Baum, J. Barnes, Viking Orbiter imaging Observations of Dust in the Martian Atmosphere, *J. Geophys. Res.*, 84 (B6), 2795-2820, 1979.

Capen, C. F., and L. J. Martin, The developing stages of the Martian yellow storm of 1971, *Lowell Obs. Bull.*, 7(157), 211-216, 1971.

Chase, S. C., Jr., J. L. Engel, H. W. Eyerly, H. H. Kieffer, F. D. Palluconi, and D. Schofield, Viking infrared thermal mapper, *App. Optics*, 17 (8), 1243-1251, 1978.

Chassefiere, E., J. E. Blamont, V. A. Krasnopolsky, O. I., Korablev, S. K. Atreya, R. A. West, Vertical structure and size distribution of Martian aerosols from solar occultation measurements, *Icarus*, 97 (1), 46-69, 1992.

Christensen, P. R., Martian dust mantling and surface composition: Interpretation of thermophysical properties, *J. of Geophys. Res.*, 87 (B12), 9985-9998, 1982.

Christensen, P. R., Variations in Martian surface composition and cloud occurrence determined from thermal infrared spectroscopy: analysis of Viking and Mariner 9 data, *J. Geophys. Res.*, 103 (E1), 1733-1746, 1998.

Christensen, P. R. and R. W. Zurek, Martian North Polar Hazes and Surface Ice: Results From the Viking Survey/ Completion Mission, *J. Geophys. Res.*, 89 (B6), 4587-4596, 1984.

Christensen, P. R., D. L. Anderson, S. C. Chase, R. N. Clark, H. H. Kieffer, M. C. Malin, J. C. Pearl, J. Carpenter, N. Bandiera, F. G. Brown, S. Silverman, Thermal Emission Spectrometer Experiment: Mars Observer Mission, *J. Geophys. Res.*, 97 (E5), 7719-7734, 1992.

Clancy, R. T., S. W. Lee, G. R. Gladstone, W. W. McMillan, and T. Rousch, A new model for Mars atmospheric dust based upon analysis of ultraviolet through infrared observations from Mariner 9, Viking, and Phobos, *J. Geophys. Res.*, 100 (E3), 5251-5263, 1995.

Clancy, R. T., *et al.*, Water Vapor Saturation at Low Altitudes around Mars Aphelion: A Key to Mars Climate?, *Icarus*, 122, 36-62, 1996.

Curran, R. J., B. J. Conrath, R. A. Hanel, V. G. Kunde, J. C. Pearl, Mars: Mariner 9 Spectroscopic Evidence for H₂O Ice Clouds, *Science*, 183, 381-383, 1973.

Davies, D. W., The vertical distribution of Mars water vapour, *J. Geophys. Res.*, 84 (B6), 2875-9, 1979.

Deirmendjian, D., Electromagnetic Scattering on Spherical Polydispersions, American Elsevier, New York, 77-83, 1969.

French, R. G., P. J. Gierasch, B. D. Popp, and R. J. Yerdon, Global patterns in cloud forms on Mars, *Icarus*, 45, 468-493, 1981.

Haberle, R. M., and B. M. Jakosky, Sublimation and transport of water from the north residual polar cap on Mars, *J. Geophys. Res.*, 95, 1423-1437, 1990.

Hartmann, W. K., Mars: Topographic Control of Clouds, 1907-1973, *Icarus*, Vol. 33, pp. 380-387, 1978.

Hollingsworth, J. L., R. M. Haberle, J. R. Barnes, A. F. C. Bridger, J. B. Pollack, H. Lee, J. Schaeffer, Orographic control of storm zones on Mars, *Nature*, Vol. 380, pp. 413-416, April 4, 1996.

Hollingsworth, J. L., R. M. Haberle, J. Schaeffer, Seasonal variations of storm zones on Mars, *Adv. Space Res.*, Vol. 19, No. 8, pp. 1237-1240, 1997.

Houben, H., R. M. Haberle, R. E. Young, A. P. Zent, Modeling the Martian seasonal water cycle, *J. Geophys. Res.*, Vol. 102, No. E4, pp. 9069-9083, April 25, 1997.

Hunt, G. E., Thermal Infrared Properties of the Martian Atmosphere 4. Predictions of the Presence of Dust and Ice Clouds From Viking IRTM Spectral Measurements, *J. Geophys. Res.*, Vol. 84, No. B6, pp. 2865-2874, June 10, 1979.

Jakosky, B. M., The seasonal cycle of water on Mars, *Space Sci. Rev.*, 41, 131-200, 1985.

Jakosky, B. M., and R. M. Haberle, The seasonal behavior of water on Mars in *Mars*, Kieffer *et al.*, eds., The Univ. of AZ press, pp. 969-1016, 1992.

James, P. B., R. T. Clancy, S. W. Lee, L. Martin, R. Kahn, R. Zurek, R. Singer, E. Smith, Monitoring Mars with the Hubble Space Telescope: 1990-1991 observations, *Icarus*, Vol. 109, pp. 79-101, 1994.

James, P. B., J. F. Bell III, R. T. Clancy, S. W. Lee, L. J. Martin, M. J. Wolff, Global imaging of Mars by Hubble space telescope during the 1995 opposition, *J. of Geophys. Res.*, Vol. 101, No. E8, pp. 18883-18890, Aug. 25, 1996.

Jaquin, F., P. Gierasch, R. Kahn, The Vertical Structure of Limb Hazes in the Martian Atmosphere, *Icarus*, Vol. 68, pp. 442-461, 1986.

Kahn, R., The Spatial and Seasonal Distribution of Martian Clouds and Some Meteorological Implications, *J. Geophys. Res.*, Vol. 89, No. A8, pp. 6671-6688, Aug. 1, 1984.

Kahn, R., Ice haze, snow, and the Mars water cycle, *J. Geophys. Res.*, Vol. 95, No. B9, pp. 14677-93, 30 Aug., 1990.

Leovy, C. B., G. A. Briggs, A. T. Young, B. A. Smith, J. B. Pollack, E. N. Shipley, R. L. Wildey, The Martian Atmosphere: Mariner 9 Television Experiment Progress Report, *Icarus*, Vol. 17, pp. 272-292, 1972.

Malin, M. C., G. E. Danielson, A. P. Ingersoll, H. Masursky, J. Veverka, M. A. Ravine and T. A. Soulanille, The Mars Observer Camera, *J. Geophys. Res.*, Vol. 97, No. E5, pp. 7699-7718, 1992.

Martin, L. J. and R. W. Zurek, An analysis of the History of Dust activity on Mars, *J. Geophys. Res.*, Vol. 98, No. E2, pp. 3221-3246, 1993.

Martin, T. Z., Thermal Infrared Opacity of the Mars Atmosphere, *Icarus*, 66, pp. 2-21, 1986.

Martin, T. Z., and M. I. Richardson, New dust opacity mapping from Viking infrared thermal mapper data, *J. Geophys. Res.*, Vol. 98, No. E6, pp. 10941-10949, 1993.

McCleese, D. J., R. D. Haskins, J. T. Schofield, R. W. Zurek, C. B. Leovy, D. A. Paige, and F. W. Taylor, Atmosphere and climate studies of Mars using the Mars Observer Pressure Modulator Infrared Radiometer, *J. Geophys. Res.*, 97 (E5), 7735-7757, 1992.

Paige, D. A., J. E. Bachman, K. D. Keegan, Thermal and albedo mapping of the polar regions of Mars using Viking thermal mapper observations. 1. North polar region, *J. Geophys Res.*, Vol. 99, No. E12, pp. 25959--91, 25 Dec. 1994.

Palluconi, F. D., and H. H. Kieffer, Thermal Inertia Mapping of Mars from 60°S to 60°N, *Icarus*, Vol. 45, pp. 415-426, 1981.

Pleskot, L. K., and E. D. Miner, Time variability of the Martian bolometric albedo, *Icarus*, Vol. 45, No. 1, pp. 179-201, Jan. 1981.

Richardson, M. I., Comparison of microwave and infrared measurements of Martian atmospheric temperatures: Implications for short-term climate variability, *J. Geophys. Res.*, 103 (E3), 5911-5918, 1998.

Roush, T., J. Pollack, and J. Orenberg, Derivation of midinfrared (5-25 μm) optical constants of some silicates and plagonite, *Icarus*, 94 (1), 191-208, 1991.

Slipher, E. C., Mars: The photographic story, Northland Press, Flagstaff, AZ and Sky Publishing Corporation, Cambridge, MA, 1962.

Smith, P. H., J. F. Bell III, N. T. Bridges, D. T. Britt, L. Gaddis, R. Greeley, H. U. Keller, K. E. Herkenhoff, R. Jaumann, J. R. Johnson, R. L. Kirk, M. Lemmon, J. N. Maki, M. C. Malin, S. L. Murchie, J. Oberst, T. J. Parker, R. J. Reid, R. Sablotny, L. A. Soderblom, C. Stoker, R. Sullivan, N. Thomas, M. G. Tomasko, W. Ward, E. Wegryn, Results from the Mars Pathfinder Camera, *Science*, Vol. 278, pp. 1758-1765, 5 December, 1997.

Smith, S. A., B. A. Smith, Diurnal and Seasonal Behavior of Discrete White Clouds on Mars, *Icarus*, Vol. 16, pp. 509-521, 1972.

Snook, K., Optical Properties and Radiative Heating Effects of Dust Suspended in the Mars Atmosphere, Thesis for the Department of Aeronautics and Astronautics, Stanford University, March 1999.

Snyder, C. W., The Missions of the Viking Orbiters, *J. Geophys. Res.*, Vol. 82, No. 28, pp. 3971-3982, Sept. 30, 1977.

Snyder, C. W., and V. I. Moroz, Spacecraft Exploration of Mars in *Mars*, Keiffer *et al.*, eds., The Univ. of AZ press, pp. 71-119, 1992.

Toon, O. B., J. B. Pollack, and C. Sagan, Physical Properties of the Particles Composing the Martian Dust Storm of 1971-1972, *Icarus*, Vol. 30, pp. 663-696, 1977.

Wilson, R. J. and M.I. Richardson, The martian atmosphere during the Viking mission, 1: Infrared measurements of atmospheric temperatures revisited, *Icarus*, accepted, 1999.

Wood, S. E., M. I. Richardson, R. J. Wilson, D. A. Paige, Tropical CO₂ clouds on Mars: microphysics and radiative effects, 1997 Fall AGU meeting, *EOS*, Vol. 78, supplement, p. F411.

Zurek, R. W., Comparative aspects of the climate of Mars: An introduction to the current atmosphere in *Mars*, Keiffer *et al.*, eds., The Univ. of AZ press, pp. 813-816, 1992.

Zurek, R. W. and L. J. Martin, Interannual variability of Planet-Encircling Dust Storms on Mars, *J. Geophys. Res.*, Vol. 98, No. E2, pp. 3427-3259, 1993.

Zurek, R. W., J. R. Barnes, R. M. Haberle, J. B. Pollack, J. E. Tillman, and C. B. Leovy, Dynamics of the Atmosphere of Mars in *Mars*, Keiffer *et al.*, eds., The Univ. of AZ press, pp. 835-933, 1992.

Acknowledgements

LKT would like to thank R. Zurek and D. Paige for valuable scientific discussions, L. Barnard for assistance in figure preparation, and D. Bass for a careful review of a previous draft of this manuscript. This research was supported by a NASA grant.